Banner appropriate to article type will appear here in typeset article

A hierarchical decomposition of internal wave fields

Thomas E. Dobra[1,2], Andrew G. W. Lawrie[1] † and Stuart B. Dalziel[2]

[1]Hele-Shaw Laboratory, University of Bristol, University Walk, Bristol, BS8 1TR, UK

[2]Department of Applied Mathematics and Theoretical Physics, University of Cambridge, Wilberforce Road, Cambridge, CB3 0WA, UK

(Received xx; revised xx; accepted xx)

Internal gravity wave fields are decomposed into temporal modes revealing the hierarchical structure of nonlinear wave–wave interactions. We present a novel fusion of Green's functions for solving the forced internal wave equation with a weakly nonlinear perturbation expansion. Our approach is semi-analytical, based on integration over finite elements with the perturbation expansion ensuring source terms at each order are only dependent on the solutions at lower orders. Thus, the procedure is purely inductive and efficient to compute. To perform a thorough validation of our new method, we diagnose experiments using Synthetic Schlieren and apply sophisticated post-processing techniques, including Dynamic Mode Decomposition, to obtain these temporal modes for systems with discrete input frequencies. By decomposing the experimental field and comparing individual constituents against equivalents synthesised by our model, we are able to present the first truly comprehensive, validated, mechanistic picture of wave–wave interactions to arbitrary order. This synergy enables us to identify non-wave oscillatory behaviour at frequencies shared by waves in the hierarchy and leads us to discover an important open question regarding transmission efficiency within individual wave–wave interactions. Although our experiments are generated by boundary displacements, we present equivalences between source terms and boundary displacements so that the class of applicable systems may be broadened. Our technique also generalises to aperiodic and unbounded configurations and to any weakly nonlinear wave-governed system for which there is an available Green's function.

Key words: Internal waves, Ocean processes, Stratified flows, Topographic effects, Computational methods, Wave scattering, Solitary waves

1. Introduction

The interior of the oceans may be considered as a vast field of internal gravity waves. Continuous stratification, gravitational forcing due to the lunar orbit (Rattray 1960) and suitable bathymetry conspire to produce a complex interior system of mechanical wave transmission. Amplitudes of these waves may be hundreds of metres (Susanto *et al.* 2005), but they are known to propagate at shallow angles and in beam-like geometric patterns. In

† Email address for correspondence: andrew.lawrie@bristol.ac.uk

Abstract must not spill onto p.2

general, waveforms are modified by boundary topography (van Haren *et al.* 2002), and in particular, their spectral form is crucial to predicting their interaction. There are several well known features of internal wave mechanics that arise due to nonlinearity in the underlying physics, and primarily these arise from the quadratic structure of the advection operator. Viewed in spectral space, the advection operator may be cast as a geometric relationship between wavevectors and frequencies known as triadic interaction (Phillips 1960; Thorpe 1966). Special cases include the interaction of two crossing wave beams (McComas & Bretherton 1977; Sun & Kunze 1999*a*,*b*; Javam *et al.* 2000; Tabaei *et al.* 2005; Smith & Crockett 2014), triadic resonant instability (Davis & Acrivos 1967; Martin *et al.* 1969; McEwan 1971; Bourget *et al.* 2013) and a limiting case known as parametric subharmonic instability (McEwan & Robinson 1975; Benielli & Sommeria 1998; Koudella & Staquet 2006; Karimi & Akylas 2014). We will discuss in depth interactions of crossing wave beams as part of this paper, but we refer the reader to Dauxois *et al.* (2018) for a review of instabilities and Müller *et al.* (1986) for a broader overview.

Experiments have played an important role in refining our understanding of internal wave systems ranging from early studies of oscillating cylinders (Görtler 1943; Mowbray & Rarity 1967) to complex mechanical devices for generating quasi-planar waves (McEwan 1971; Gostiaux *et al.* 2007). There are broadly three approaches to analysing wave systems: characteristics, Green's functions and Fourier methods. The oscillating cylinder is the natural analogue of characteristic (Hurley 1972) and Green's function approaches (Hurley 1969; Voisin 1991), because spatially localised beams emerge in a St. Andrew's cross pattern and these are aligned with the characteristics. On the other hand, Fourier methods more naturally correspond to quasi-planar systems (Mercier *et al.* 2010), where there is implicit spatial periodicity as well as temporal periodicity.

In this paper, we shall build a more general framework based on Green's functions and seek to validate using laboratory experiments, firstly on a polychromatic aperiodic example case of lee waves, and then develop to a case where steady, periodic wave beams show significant nonlinear interaction. The experiments utilise the unique capabilities of the "magic carpet" (Dobra *et al.* 2019) to generate a full spectrum of wave beams, Synthetic Schlieren (Dalziel *et al.* 1998; Sutherland *et al.* 1999; Dalziel *et al.* 2000; **?**) to diagnose the resulting wave field from density gradients, and Dynamic Mode Decomposition (Schmid 2010) to dissect the modal structure. Using these tools, figure 1 illustrates a typical wave–wave interaction with two incident beams in subfigures 1(*a*) and 1(*b*) with direction of propagation shown by the arrows. Subfigure 1(*c*) shows a snapshot of the experimentally observed field, and subfigures 1(*d*)–(*f*) show "daughter" modes that are observed to emerge nonlinearly from the interaction and have directions of propagation as shown.

To address the question of nonlinear wave–wave interactions, our new framework will allow for weakly nonlinear interactions between a hierarchy of Green's functions. We utilise Green's functions to represent the driving waves and derive the weakly nonlinear transfer terms that pass energy into other frequency and wavenumber components, these also being represented in terms of Green's functions. Our framework is sufficiently broad to deal not only with interactions of the form shown in figure 1 that lead to resonance (disturbances that satisfy both the geometric conditions on wavenumber and frequency and also satisfy the relevant dispersion relation) but also those where the linear dispersion relation is not satisfied.

The structure of this article is as follows. We present the background material to the governing equations in §2 and discuss the tractability of other analytical options. Focussing on the monochromatic Green's function solution to the linear equation in §3, we prepare the building blocks of a hierarchical numerical approach. In §4, we demonstrate application of this approach to inviscid, aperiodic systems, and carefully validate against experiments using

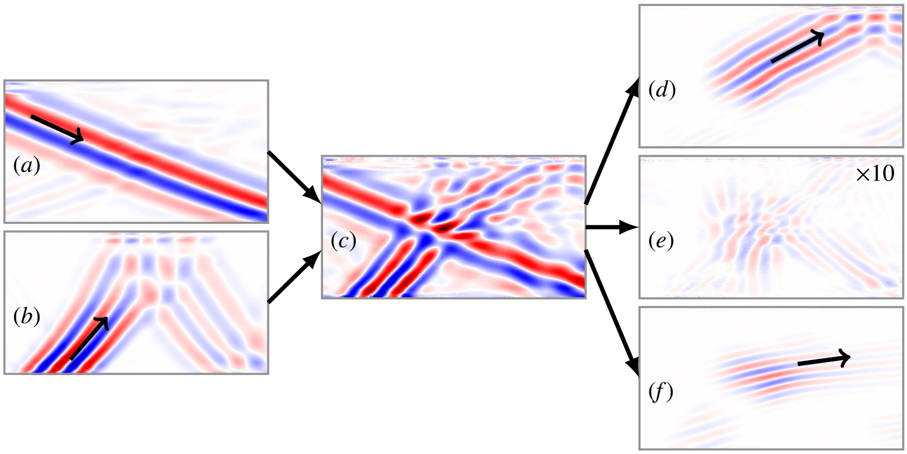

Figure 1: Schematic showing a decomposition of a wave–wave interaction between two incident internal wave beams ((*a*) and (*b*)). Subfigure (*c*) shows the full experimentally observed wave field. Subfigures (*d*)–(*f*) show nonlinearly generated "daughter" modes that are identifiable from the experiment. The arrows indicate the direction of propagation of each wave beam.

our "magic carpet" (Dobra *et al.* 2019). We then generalise in §5 our numerical Green's function approach so that we may capture the physics of nonlinearly interacting internal waves. We employ the perturbation expansion technique of Tabaei *et al.* (2005) and developed further in Dobra *et al.* (2021) to account for successive layers of wave–wave interactions and demonstrate that the resultant field compares well with experimental observations. Finally, in §6, we draw our conclusions.

2. Internal wave equation

We begin by considering two-dimensional, inviscid, linear internal waves in a quiescent, Boussinesq density stratification, $\rho_0(z)$. These restrictions closely approximate the conditions in our laboratory experiments, where it is particularly advantageous to consider flows with limited variation in the third dimension for ease of diagnosis. We define $\boldsymbol{x} = (x, z)$ as the horizontal and vertical coordinates with corresponding unit basis vectors $\{\boldsymbol{e}_x, \boldsymbol{e}_z\}$, and we assume there is no diffusion of mass or heat. Let t be time, $\boldsymbol{u} = (u, w)$ the velocity field, p' the perturbation from hydrostatic pressure, ρ_{00} be the Boussinesq reference density, ρ' (with $|\rho'| \ll \rho_{00}$) the perturbation from $\rho_0(z)$ and g gravitational acceleration. Then, the three nonlinear governing equations are the conservation of momentum (Euler equation),

$$\rho_{00}\left(\frac{\partial \boldsymbol{u}}{\partial t} + \boldsymbol{u}\cdot\boldsymbol{\nabla}\boldsymbol{u}\right) = -\boldsymbol{\nabla}p' - \rho' g\boldsymbol{e}_z, \tag{2.1}$$

the conservation of volume (equivalent to incompressibility in the case of a homogeneous fluid),

$$\boldsymbol{\nabla}\cdot\boldsymbol{u} = 0, \tag{2.2}$$

and consequently the conservation of mass may be written as

$$\frac{\partial \rho'}{\partial t} + \boldsymbol{u}\cdot\boldsymbol{\nabla}(\rho_0 + \rho') = 0. \tag{2.3}$$

In the linear wave approximation, the two nonlinear terms arising from the advection operator $\boldsymbol{u}\cdot\boldsymbol{\nabla}$ are considered to be negligible. The remaining derivative operators can be isolated into a complex matrix $\boldsymbol{P}$ that acts on a state vector $\boldsymbol{\phi}$, say, and the system arranged into homogeneous form. Taking a single Fourier mode of $\boldsymbol{\phi}$ with wavevector $\boldsymbol{k} = (k, m)$ and frequency ω, we can write

$$\boldsymbol{\phi} = \hat{\boldsymbol{\phi}}\, e^{\mathrm{i}(\boldsymbol{k}\cdot\boldsymbol{x}-\omega t)}. \tag{2.4}$$

The derivative operator, $\boldsymbol{P}$, then takes the complex algebraic form $\hat{\boldsymbol{P}}$. For a homogeneous system, non-trivial symmetries are found when the determinant $|\hat{\boldsymbol{P}}| = 0$, and these correspond to resonant wave behaviours. From

$$\left|\hat{\boldsymbol{P}}\right| = \omega^2 - \left(-\frac{g}{\rho_{00}}\frac{\mathrm{d}\rho_0}{\mathrm{d}z}\right)\frac{k^2}{|\boldsymbol{k}|^2} = 0 \tag{2.5}$$

arises a natural frequency, the buoyancy (Brunt–Väisälä) frequency,

$$N = \sqrt{-\frac{g}{\rho_{00}}\frac{\mathrm{d}\rho_0}{\mathrm{d}z}}, \tag{2.6}$$

and by examining the geometry of $k/|\boldsymbol{k}|$, the dispersion relation,

$$\omega = N\cos\Theta, \tag{2.7}$$

is obtained, where Θ is the angle between wavevector $\boldsymbol{k}$ and the horizontal. Since this system is linear, any perturbation quantity χ satisfies the dispersion relation provided that

$$\left(\omega^2|\boldsymbol{k}|^2 - N^2k^2\right)\hat{\chi} = 0. \tag{2.8}$$

Taking the inverse Fourier transform yields the linear internal wave equation,

$$\left(\frac{\partial^2}{\partial t^2}\nabla^2 + N^2\frac{\partial^2}{\partial x^2}\right)\chi = \mathcal{L}\chi = 0, \tag{2.9}$$

where we define $\mathcal{L}$ to be the corresponding operator. From any choice of χ, the polarisation of any other quantity can be derived by appropriate substitution into the linearised equations. In particular, any such quantity will also satisfy the linear internal wave equation.

Source terms may be configured to be equivalent to the action of boundaries, and we will see in §5 that they can also inductively account for discrepancies between a linear wave approximation and the corresponding nonlinear field. Thus, we consider solution approaches to the inhomogeneous internal wave equation, $\mathcal{L}\chi = f$, with source distribution $f(\boldsymbol{x}, t)$.

While we could choose to work with any variable χ, it is important to select a representation of the system that has a clear physical interpretation. In view of this, two interesting choices of χ are an internal potential, ξ, as used by Voisin (1994) and Scase & Dalziel (2004), and the streamfunction, ψ. We now consider the physical interpretation of point source terms for each of these potentials in turn.

The internal potential is defined by

$$\boldsymbol{u} = \left(\frac{\partial^2}{\partial t^2}\boldsymbol{\nabla} + N^2\boldsymbol{e}_x\frac{\partial}{\partial x}\right)\xi = \left(\left(\frac{\partial^2}{\partial t^2} + N^2\right)\frac{\partial\xi}{\partial x}, \frac{\partial^3\xi}{\partial t^2\,\partial z}\right), \tag{2.10}$$

and is chosen such that $\boldsymbol{\nabla}\cdot\boldsymbol{u} = \mathcal{L}\xi$. We consider an instantaneous point source of unit strength at $\boldsymbol{x}_0$ that is active at time t_0, expressed in terms of Dirac-δ functions as $f = \delta(\boldsymbol{x}-\boldsymbol{x}_0)\,\delta(t-t_0)$. Integrating along a short time interval including t_0 over some fixed volume V around $\boldsymbol{x}_0$ with boundary ∂V and using the divergence theorem gives

$$\int_{t_0-\epsilon}^{t_0+\epsilon}\int_V f\,\mathrm{d}V\,\mathrm{d}t = \int_{t_0-\epsilon}^{t_0+\epsilon}\int_V \mathcal{L}\xi\,\mathrm{d}V\,\mathrm{d}t = \int_{t_0-\epsilon}^{t_0+\epsilon}\int_{\partial V} \boldsymbol{u}\cdot\mathrm{d}\boldsymbol{S}\,\mathrm{d}t, \tag{2.11}$$

which is the total volume of fluid ejected through enclosing surface, S. Therefore, the point source injects one unit of fluid volume.

The streamfunction, ψ, is an integral of the velocity field according to

$$\boldsymbol{u} = \boldsymbol{\nabla}\times\left(\psi\boldsymbol{e}_y\right) = \left(-\frac{\partial\psi}{\partial z}, \frac{\partial\psi}{\partial x}\right). \tag{2.12}$$

It follows immediately that the vorticity $\boldsymbol{\nabla}\times\boldsymbol{u} = -\nabla^2\psi$, and it appears in the first term of the internal wave equation (2.9) if we set $\chi = \psi$. Expressing the linear terms of (2.3) in terms of ψ, multiplying by g/ρ_{00} and differentiating with respect to x, we obtain

$$N^2\frac{\partial^2\psi}{\partial x^2} = \frac{g}{\rho_{00}}\frac{\partial^2\rho'}{\partial x\,\partial t}. \tag{2.13}$$

The left-hand side appears in (2.9) and so we may integrate with respect to t to obtain the vorticity equation,

$$-\frac{\partial}{\partial t}\nabla^2\psi - \frac{g}{\rho_{00}}\frac{\partial\rho'}{\partial x} = 0, \tag{2.14}$$

which can also be derived directly from the linearised momentum equation. Vorticity in a fixed control volume changes only due to baroclinic generation or by the introduction of sources applied on the right-hand side of (2.14). For a source $f = \delta(\boldsymbol{x}-\boldsymbol{x}_0)\,\delta(t-t_0)$ in the internal wave equation (2.9), the corresponding vorticity source in (2.14) may be expressed in terms of the Heaviside step function, H, as $\int f\,\mathrm{d}t = \delta(\boldsymbol{x}-\boldsymbol{x}_0)\,\mathrm{H}(t-t_0)$, which we may interpret as a supply of vorticity at unit rate after t_0.

While steady-state waves in any system violate causality, they provide a good approximation to their long term behaviour, so in practice, we use monochromatic sources of the form $f = \delta(\boldsymbol{x}-\boldsymbol{x}_0)\exp(-\mathrm{i}\omega t)$. For the internal potential, ξ, the volume source is of unit amplitude and is in phase with f, and for the streamfunction, ψ, the vorticity is modified by a factor of $-\mathrm{i}/\omega$.

With any choice of χ, one candidate approach uses Fourier transforms in both time and space (denoted by a circumflex) to yield the following algebraic equation,

$$\hat{\psi} = \frac{\hat{f}}{\omega^2|\boldsymbol{k}|^2 - N^2k^2}, \tag{2.15}$$

We note however that the denominator is zero for any Fourier modes that satisfy the dispersion relation, and these correspond to resonant modes. In common with a simple harmonic oscillator, the amplitudes of resonant modes grow linearly. This growth may occur in time, however over a broad class of wave equations that exist in multiple dimensions, growth may equally occur along spatial directions, and this remains the case for any linear combination of space–time directions (Dobra 2018). Although in the internal wave system each mode is a plane wave of infinite extent, a broadband linear superposition of such modes may be configured to produce an internal wave beam in space with finite width. Counterintuitively, there exists the limiting case of steady-state resonance, where all of the energy is transported away from the source and amplitude growth is found in purely spatial directions.

Dobra (2018) combined these resonant waves with non-resonant forced oscillations to obtain an integral solution in terms of inverse Fourier transforms. However, exact solutions only apply to periodic domains, yet the experimental configurations we consider in §§4–5 are best approximated by a combination of reflecting and non-reflecting boundary conditions, which Fourier methods do not in general support. Given that an intermediate aim in §3 is to establish a numerical method with broad enough generality to handle aperiodicity in both space and time, we must explore alternative techniques for a computationally efficient implementation.

One such approach uses a suitably chosen Green's function, encoding the system response to a point source. A distribution of point sources in space and time may be configured to represent an arbitrary excitation of the system, and in this work we consider distributions that produce interference patterns representing both boundary displacements and mode–mode interactions. For the simplest point source, $f = \delta(\boldsymbol{x} - \boldsymbol{x}_0)\,\delta(t - t_0)$, Sekerzh-Zen'kovich (1981) derived the instantaneous Green's function by Fourier transforming in space only, solving the resulting ordinary differential equation in time and taking the inverse transform. Once again, however, we have non-vanishing solutions at the boundary, and in any finite domain (such as one requires to compute an approximate numerical solution), the Green's function obtained using Fourier techniques encodes the response to a periodic array of isolated point sources. By instead using a sustained monochromatic source, $f = \delta(\boldsymbol{x} - \boldsymbol{x}_0)\exp(-\mathrm{i}\omega t)$, we will obtain a solution in terms of elementary functions (see §3), so we will avoid difficulties with non-vanishing solutions at the boundary.

3. Monochromatic Green's function

3.1. *Analysis*

The monochromatic Green's function, $G_\omega(\boldsymbol{x};\boldsymbol{x}_0)$, is the solution to the internal wave equation with point forcing as given by

$$\left(\frac{\partial^2}{\partial t^2}\nabla^2 + N^2\frac{\partial^2}{\partial x^2}\right)G_\omega \exp(-\mathrm{i}\omega t) = \delta(\boldsymbol{x} - \boldsymbol{x}_0)\exp(-\mathrm{i}\omega t). \tag{3.1}$$

Provided we have a solution for G_ω, the solution to the internal wave equation with source distribution of the form $f = f_\omega(x, z)\exp(-\mathrm{i}\omega t)$ is

$$\chi_\omega(\boldsymbol{x}) = \int_{\mathbb{R}^2} G_\omega(\boldsymbol{x};\boldsymbol{x}_0)\, f_\omega(\boldsymbol{x}_0)\,\mathrm{d}^2\boldsymbol{x}_0, \tag{3.2}$$

where $\mathbb{R}$ is the set of real numbers.

The precise form of the Green's function depends on the configuration of the domain and boundary conditions. In the well-studied case of internal tides (e.g. Robinson 1969; Pétrélis *et al.* 2006; Balmforth & Peacock 2009), the appropriate Green's function takes the form of a sum of normal modes. However, this is less general than the spatially unbounded case considered by Voisin (1991), who presented a comprehensive derivation of the three-dimensional Green's functions. His work considered both instantaneous and monochromatic sources and considers in some depth the implications for causality of using Green's functions for internal waves. Motivated by physical arguments, earlier work by Hurley (1969) quoted the two-dimensional streamfunction due to a monochromatic point vorticity source, which we identify as $-\mathrm{i}\omega G_\omega$ in our own work, but this does not include the instantaneous source solution we discussed at the end of §2. This is important because instantaneous sources are potentially an attractive foundation for a semi-analytical model with sufficient generality to study both wave and non-wave perturbations to a density field. Unfortunately, there is no numerical method for an unbounded Fourier transform, and there are concerns over causality in the spatially periodic domain that we would require for a corresponding numerical method. The simplest causal foundation is the monochromatic source. We note in addition that both

Hurley and Voisin use exponential, rather than linear, density stratifications. The exponential form leads to a distinct interpretation of the buoyancy frequency, N, and the linear wave equation includes an additional term arising from the curvature of the stratification. The solutions are related by a conformal map. Given these points and further technical intricacies that are specific to the two-dimensional case and influenced our choice of integration scheme, there is some justification for presenting our own solution in preparation for a flexible, general numerical implementation.

Our solution approach is summarised as follows, with full details in appendix A. Evaluating the time derivatives in (3.1), defining the constant $\Gamma = (1 - (N/\omega)^2)^{1/2}$ and cancelling the temporal exponential terms yields

$$\Gamma^2 \frac{\partial^2 G_\omega}{\partial x^2} + \frac{\partial^2 G_\omega}{\partial z^2} = -\frac{\delta(\boldsymbol{x} - \boldsymbol{x}_0)}{\omega^2}. \tag{3.3}$$

We note that Γ is real for evanescent internal waves, $|\omega| > N$, but is imaginary for $|\omega| < N$. For $\Gamma \in \mathbb{R}$, this elliptic equation is a skewed Poisson's equation, and a dilatation allows us to use the free space Green's function for the unskewed Poisson's equation. Let r be the distance from the source in the transformed space so that

$$r^2 = \frac{(x - x_0)^2}{1 - \left(\frac{N}{\omega}\right)^2} + (z - z_0)^2, \tag{3.4}$$

then the standard Green's function for a source that will generate an evanescent wave is

$$G_\omega = -\frac{\log\left(r^2\right)}{4\pi\omega^2\Gamma}. \tag{3.5}$$

Analytic continuation from $|\omega| > N$ to all $\omega \in \mathbb{R}$ enables a solution to the corresponding hyperbolic equation, and wavepackets propagate along the real-valued characteristics, as discussed in Dobra *et al.* (2021). There are branch points where the argument of a logarithm or a number raised to a fractional power is zero or infinity, so the branch points are at $r^2 = \{0, \infty\}$ and $1/\Gamma = \{0, \infty\}$, which gives the branch points

$$\omega = 0, \pm \frac{N}{\sqrt{1 + \left(\frac{x - x_0}{z - z_0}\right)^2}} \text{ and } \pm N. \tag{3.6}$$

The $r^2 = 0$ branch points only occur where $|\omega| \leqslant N$ and are on the characteristics passing through $\boldsymbol{x}_0$. We assemble the Green's function for each solution region in table 3 in appendix A, where we classify by the complex argument of r^2 and $1/\Gamma$. By defining $\gamma = ((N/\omega)^2 - 1)^{1/2} = \tan\Theta$, as may be inferred from the dispersion relation (2.7), we condense all the propagating cases to

$$G_\omega = \mathrm{i}\,\mathrm{sgn}\,(\omega) \frac{\log\left|\left(\frac{x - x_0}{\gamma}\right)^2 - (z - z_0)^2\right|}{4\pi\omega^2\gamma} + \frac{1}{4\omega^2\gamma}\,\mathrm{H}\left(\left(\frac{x - x_0}{\gamma}\right)^2 - (z - z_0)^2\right). \tag{3.7}$$

For sources that generate evanescent waves, the Green's function is real, so the response is in phase with the forcing. A contour plot of the Green's function is shown in figure 2. As $\omega \to \infty$, or equivalently as $N \to 0$, the elliptical contours broaden to become circular. In the limiting case, this is the unstratified potential flow response corresponding to our choice of χ. The contours of the streamfunction, ψ, always represent streamlines in the flow, whereas only in the case when the internal potential, ξ, is monochromatic and $N = 0$ do its contours coincide with those of the velocity potential, ϕ, as defined by $\boldsymbol{u} = \boldsymbol{\nabla}\phi$. The

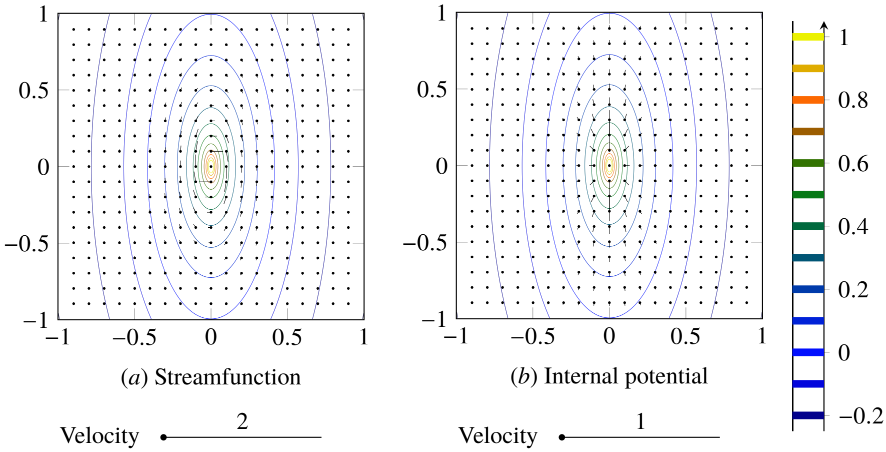

Figure 2: Real component of the evanescent Green's function for $\omega = 1.1N$, which shows (a) the streamlines and (b) contours of the internal potential, and the derived velocity fields at $t = 0$. The velocity indicators have been scaled for plotting. The potentials and their corresponding fluid speeds grow unboundedly at the origin. The imaginary part is identically zero.

fundamental streamfunction flow is a monochromatic point vortex, whereas for the internal potential, it is a monochromatic volume source.

For $|\omega| < N$, we obtain propagating solutions with characteristics of gradient $\pm 1/\gamma$. The imaginary part of the Green's function for $\omega = 0.5N$ is plotted in figure 3. The real part is piecewise constant with discontinuities across the characteristics. When $|x - x_0| > \gamma |z - z_0|$, the real part equals $1/(4\omega^2\gamma)$ and equals zero elsewhere. We see a St. Andrew's Cross pattern analogous to that produced by a small cylinder undergoing vertical oscillations (Görtler 1943; Mowbray & Rarity 1967). The potential and derived velocities grow unboundedly on approaching the characteristics, which is a consequence of the idealisations embedded in this model. Nonetheless, when integrated over point sources of zero area, a finite contribution is obtained in the same way that an integration over δ-functions produces a finite integral, a property we will exploit in §3.2.

For $|\omega| < N$, the logarithm can be decomposed into two characteristic coordinates,

$$\eta_\pm = \left(\frac{x - x_0}{\gamma}\right) \mp (z - z_0), \tag{3.8}$$

such that the η_+ characteristics have positive slope and η_- negative. The argument of the logarithm, $\left|r^2\right|$, becomes a difference of squares because $\Gamma^2 < 0$, so decomposes into the characteristic coordinates,

$$\left|r^2\right| = \left|\left[\left(\frac{x - x_0}{\gamma}\right) - (z - z_0)\right]\left[\left(\frac{x - x_0}{\gamma}\right) + (z - z_0)\right]\right| = |\eta_+\eta_-|. \tag{3.9}$$

Therefore, the logarithm splits into two linearly superposed components with no cross term,

$$\log\left|r^2\right| = \log|\eta_+| + \log|\eta_-|. \tag{3.10}$$

The solution to a cylinder undergoing small vertical oscillations shares this decoupling into $\eta_\pm$ components (Hurley 1997). In the critical limit $\omega \to N$ from below, the characteristics are vertical, which smoothly transition to the ellipses of contours with infinite aspect ratio in the limit $\omega \to N$ from above.

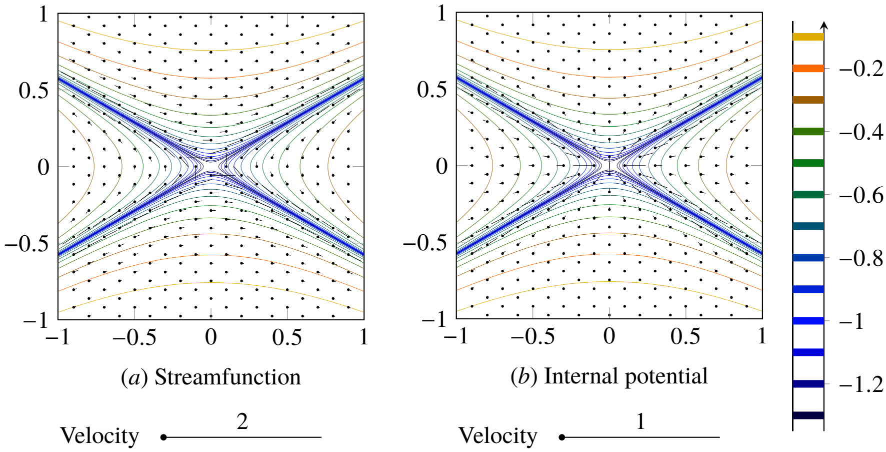

Figure 3: Imaginary component of the propagating Green's function for $\omega = 0.5N$, which shows (a) the streamlines and (b) contours of the internal potential, and the derived velocity fields at time $t = \pi/(2\omega)$. The velocity indicators have the same scale as those in the evanescent case (figure 2). The potentials and corresponding fluid speeds grow unboundedly at the characteristics, with the largest ones, which would only be visible near the origin, omitted for clarity. The real part is zero in the regions above both characteristics and below both characteristics, and is $1/(4\omega^2\gamma)$ in the remaining regions to the left of both characteristics and to the right of both characteristics.

3.2. *Numerical implementation*

In §3.1, we derived the Green's function for continuous independent variables and then provided an integral formula for χ_ω over the distribution of point sources (3.2) that is not tractable to compute analytically. We now seek to use our Green's function solution as the basis for a semi-analytical method to evaluate the potential, χ_ω, at arbitrary locations in space. We anticipate distributed sources, so the potential strength at any evaluation point in space will be composed of a linear superposition of solutions from all sources. Unfortunately, our solution has logarithmic singularities along the characteristics, and so any numerical method based on pointwise evaluation will suffer from unresolvable infinities. However, with careful treatment we may regularise these over finite integration elements, and thus we discretise the domain into elements of size $\Delta x\,\Delta z$. We account for the effect of integrating over an element by introducing a corresponding modified discrete Green's function, $G_D(\boldsymbol{x};\boldsymbol{x}_D)$, and source distribution, $f_D(\boldsymbol{x}_D)$, where the centres of such elements are at $\boldsymbol{x}_D$, so that

$$\chi_\omega(\boldsymbol{x}) = \sum_{\boldsymbol{x}_D} G_D(\boldsymbol{x};\boldsymbol{x}_D)\, f_D(\boldsymbol{x}_D). \tag{3.11}$$

While much of what follows is required to determine G_D, we may simply take $f_D(\boldsymbol{x}_D) = (1/(\Delta x\,\Delta z)) \iint f_\omega(\boldsymbol{x}_0)\,\mathrm{d}^2\boldsymbol{x}_0$, integrated over the element. For smooth source distributions, we make the approximation $f_D(\boldsymbol{x}_D) \approx f_\omega(\boldsymbol{x}_D)$. If instead there is an isolated δ-function source of strength q that lies somewhere within the element, the mean source density is $f_D = q/(\Delta x\,\Delta z)$. Correspondingly, a smooth line source distribution of the form $f_\omega = q(x)\,\delta(z - z_0)$ has mean density $f_D \approx q(x_D)/\Delta z$.

We note in passing that a transformed coordinate system in (η_+, η_-) aligns with the characteristic directions of propagating waves, $|\omega| < N$, but no single coordinate system would be optimal for a polychromatic wave field as highlighted in §4. Thus, we opt to discretise a regular Cartesian grid in (x, z).

The Green's function only depends on the displacement from the source to the evaluation point, so by moving the reference frame to the centre of the finite element enclosing the source, $\boldsymbol{x}_D$, we may define a continuous variable $\boldsymbol{x}' = \boldsymbol{x} - \boldsymbol{x}_D$ over which we may integrate to determine G_D for all elements. Since the grid is regular, then for a given frequency we only need to calculate the Green's function once for each relative displacement. Then, we translate the resulting array of values according to $\boldsymbol{x}_D$ when evaluating the summation for χ_ω (3.11), truncating any values that fall outside the numerical domain.

We choose approximate formulae for each element in the Green's function matrix, G_D, according to the classification in figure 4. The figure only shows elements in the first quadrant, with the other quadrants deduced by symmetry. In the remainder of this section, we explain the decision points and formulae referenced in the figure.

Except at the source and elsewhere near its characteristics, the continuous Green's function is regular and may be approximated by a Riemann sum of the form

$$G_D(\boldsymbol{x};\boldsymbol{x}_D) \approx G_\omega(\boldsymbol{x};\boldsymbol{x}_D)\,\Delta x\,\Delta z. \tag{3.12}$$

For $|\omega| > N$, the only singular element is that which encloses $\boldsymbol{x}' = \boldsymbol{0}$, and in this case the integral is given by

$$G_D(\boldsymbol{x}_D;\boldsymbol{x}_D) = \int_{-\Delta x/2}^{\Delta x/2}\int_{-\Delta z/2}^{\Delta z/2} -\frac{\log\left(\left(\frac{x'}{\Gamma}\right)^2 + z'^2\right)}{4\pi\omega^2\Gamma}\,\mathrm{d}z'\,\mathrm{d}x'. \tag{3.13}$$

The dominant contribution to the integral comes from the logarithm close to the singularity, so we approximate the integral on the rectangular element by an ellipse of equivalent area. After dilatation, the radius, R, of the resulting circle is given by $\pi R^2 = \Delta x\,\Delta z/\Gamma$. We re-express the Green's function in polar coordinates,

$$G_D(\boldsymbol{x}_D;\boldsymbol{x}_D) \approx \int_0^{2\pi}\int_0^R -\frac{\log\left(r^2\right)}{4\pi\omega^2\Gamma} r\,\mathrm{d}r\,\mathrm{d}\theta. \tag{3.14}$$

Integration by parts gives

$$G_D(\boldsymbol{x}_D;\boldsymbol{x}_D) \approx \frac{\Delta x\,\Delta z}{4\pi\omega^2\Gamma^2}\left(1 - \log\frac{\Delta x\,\Delta z}{\pi\Gamma}\right). \tag{3.15}$$

For the case where internal waves may be generated, $|\omega| < N$, the imaginary part of the Green's function decomposes into the sum of two linearly independent components (3.10), one for each characteristic direction. Using symmetry, singular elements along the x' or z' axes intersect both characteristics (the case of two characteristics in figure 4). Conversely, singular elements away from the axes may only intersect one characteristic. We calculate each $\eta_\pm$ component of G_D separately and then add them together. For elements significantly away from the corresponding characteristic, $\eta_\pm = 0$, the component of the Green's function varies approximately linearly across the element and we invoke the centre-value approximation for a regular point (3.12). Otherwise, when the characteristic passes through an element or close to one of its corners, we approximate this component of G_D using integrals as follows.

Let us consider the η_+ component for a singular element, and define η_R and η_L to be the maximum and minimum values respectively of $\eta_+ = x'/\gamma - z'$ in this element. The displacement of the element, $\boldsymbol{x}'$, is defined by the position of its centre. Because the level sets of η_+ are lines of positive gradient and η_+ is increasing in x', the maximum value of η_+

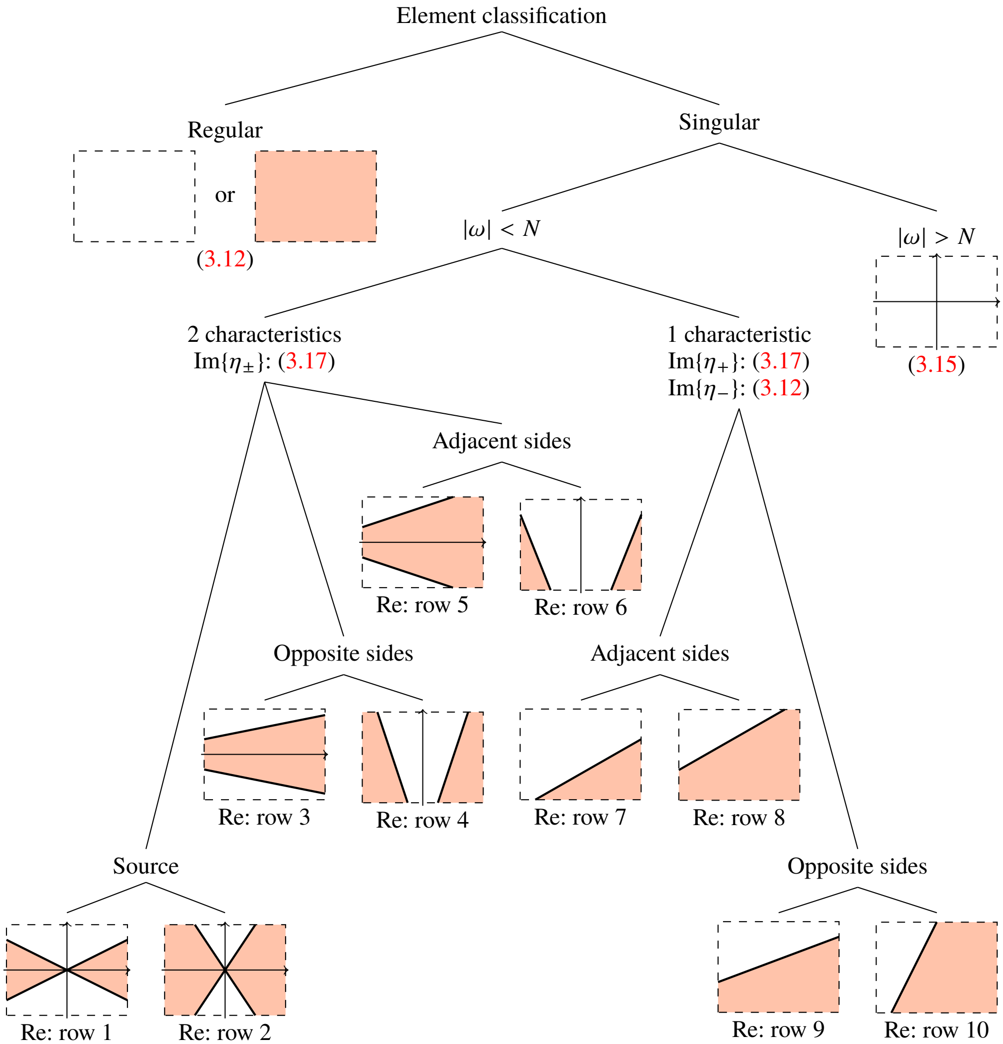

Figure 4: Classification of finite element types in the first quadrant showing the breakdown according to whether G_ω remains finite within the element, whether propagating or evanescent and by the geometry of the intersections between characteristics and the element boundary. The thumbnail images show Re$\{G_\omega\}$, which equals $1/(4\omega^2\gamma)$ in the shaded regions and zero elsewhere. Formulae for evaluating G_D are given for each case, and the areas for calculating Re$\{G_D\}$ in the propagating case are referenced by their row numbers in table 1.

occurs in the bottom-right corner of the element and the minimum in the top-left corner, so

$$\eta_R = \eta_+\left(x' + \frac{\Delta x}{2}, z' - \frac{\Delta z}{2}\right) = \frac{x' + \frac{\Delta x}{2}}{\gamma} - \left(z' - \frac{\Delta z}{2}\right), \tag{3.16a}$$

$$\eta_L = \eta_+\left(x' - \frac{\Delta x}{2}, z' + \frac{\Delta z}{2}\right) = \frac{x' - \frac{\Delta x}{2}}{\gamma} - \left(z' + \frac{\Delta z}{2}\right). \tag{3.16b}$$

We approximate the contribution across the element by integrating over a rectangle aligned with the characteristic that intersects the element corners where $\eta_+ = \eta_R$ and $\eta_+ = \eta_L$, and then scale the value by the ratio of areas. The contribution to G_D is approximately

$$\begin{aligned}\left(\frac{\Delta x\,\Delta z}{|\eta_R-\eta_L|}\right)&\left(\frac{\mathrm{i}}{4\pi\omega^2\gamma}\int_{\eta_L}^{\eta_R}\log|\eta_+|\,\mathrm{d}\eta_+\right)\\&=\left(\frac{\Delta x\,\Delta z}{|\eta_R-\eta_L|}\right)\left(\frac{\mathrm{i}}{4\pi\omega^2\gamma}\right)\Big(\eta_R(\log|\eta_R|-1)-\eta_L(\log|\eta_L|-1)\Big),\end{aligned} \tag{3.17}$$

after integration by parts, where we clarify that $\eta\log\eta=0$ when $\eta=0$. By symmetry, the same expression holds for the singular contribution due to η_- terms.

This leaves the real part of G_ω to consider. It is only nonzero in the regions to the left and to the right of the source bounded by the characteristics, which are shown for the first quadrant as shaded regions in figure 4. The real part of the integral over the element is given by $1/(4\omega^2\gamma)$ multiplied by the shaded area. We present in table 1 the formulae for all permutations of shaded area expressed in the $\boldsymbol{x}'$ coordinate system centred on an element.

4. Application to aperiodic configurations

4.1. *Introduction*

Internal waves are frequently generated by moving boundaries. For example, in the laboratory, McEwan (1971, 1973) used articulated paddles and Gostiaux *et al.* (2007) used rotating cams, but these are best suited to monochromatic excitations. We installed a “magic carpet” (Dobra *et al.* 2019) in the base of our tank, which has more general possibilities for excitation. Likewise, we generalise our numerical method for a single frequency, $\chi_\omega\exp(-\mathrm{i}\omega t)$, described in §3 to those that have a continuous spectrum of frequencies.

For a distribution of sources $f(x,z,t)=\int f_\omega(x,z)\,\exp(-\mathrm{i}\omega t)\,\mathrm{d}\omega$, we may write

$$\chi(\boldsymbol{x},t)=\int_{\mathbb{R}}\exp(-\mathrm{i}\omega t)\iint_{\mathbb{R}^2}G_\omega(\boldsymbol{x};\boldsymbol{x}_0)\,f_\omega(\boldsymbol{x}_0)\,\mathrm{d}^2\boldsymbol{x}_0\,\mathrm{d}\omega. \tag{4.1}$$

Our numerical method allows replacement of these integrals with the discrete Fourier transform, and thus we may approximate general wave fields. We summarise our procedure in algorithm 1. In the special case of a discrete set of input frequencies, we no longer need to resolve the Fourier transform and all the frequencies can be represented exactly.

In our model, we consider flexible boundaries as sources of either volume or vorticity. As we saw in §2, source terms in the internal wave equation for internal potential and streamfunction represent volume and vorticity sources respectively. We now derive formulae for the source terms of both potentials, ξ and ψ, to describe each temporal mode of an arbitrary vertical displacement of a horizontal boundary.

4.2. *Representing active boundaries with finite element sources*

In both cases, we can readily derive volume fluxes for a monochromatic source of unit strength by integrating the Green’s function, so we rescale these fluxes to match a discrete physical representation of a short distance along the boundary. The rescaling factors are collectively the required distribution of sources along the entire length of the boundary. Here, we outline the method and summarise key results; see §§4.2.1–4.2.2 for full derivations. Throughout this section, all sources are at the zero-height of the magic carpet, so without loss of generality we take $z_0=0$.

We seek to determine the volume flux, $Q(t)=Q_\omega\exp(-\mathrm{i}\omega t)$, induced by a monochromatic source of unit strength across a transect of the domain. For the internal potential, the transect is a horizontal line at $z>0$ ranging from $x=-\infty$ to $+\infty$, across which the flux amplitude $Q_\omega=\frac{1}{2}$. Whereas, the corresponding transect for the streamfunction is a vertical line segment

Case		Criterion	Shaded area
1	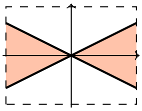	$\boldsymbol{x}' = \mathbf{0}$ $\Delta x \leqslant \gamma \Delta z$	$\frac{(\Delta x)^2}{2\gamma}$
2	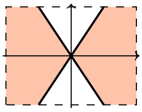	$\boldsymbol{x}' = \mathbf{0}$ $\Delta x > \gamma \Delta z$	$\Delta x\, \Delta z - \frac{\gamma(\Delta z)^2}{2}$
3	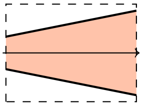	$x' \neq 0, z' = 0$ $\lvert x'\rvert + \frac{\Delta x}{2} \leqslant \gamma \frac{\Delta z}{2}$	$\frac{2\lvert x'\rvert\, \Delta x}{\gamma}$
4	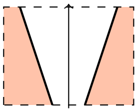	$x' = 0, z' \neq 0$ $\frac{\Delta x}{2} \geqslant \gamma(\lvert z'\rvert + \frac{\Delta z}{2})$	$\Delta x\, \Delta z - 2\gamma \lvert z'\rvert \Delta z$
5	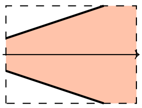	$x' \neq 0, z' = 0$ $\lvert x'\rvert - \frac{\Delta x}{2} \leqslant \gamma \frac{\Delta z}{2}$ $\lvert x'\rvert + \frac{\Delta x}{2} > \gamma \frac{\Delta z}{2}$	$\Delta x\, \Delta z - \frac{1}{\gamma}\left(\lvert x'\rvert - \frac{\Delta x}{2} - \frac{\gamma \Delta z}{2}\right)^2$
6	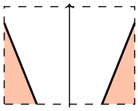	$x' = 0, z' \neq 0$ $\frac{\Delta x}{2} \geqslant \gamma(\lvert z'\rvert - \frac{\Delta z}{2})$ $\frac{\Delta x}{2} < \gamma(\lvert z'\rvert + \frac{\Delta z}{2})$	$\frac{1}{\gamma}\left(\frac{\Delta x}{2} - \gamma\left(\lvert z'\rvert - \frac{\Delta z}{2}\right)\right)^2$
7	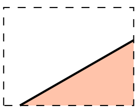	$x' \neq 0, z' \neq 0$ $\lvert x'\rvert - \frac{\Delta x}{2} \leqslant \gamma(\lvert z'\rvert - \frac{\Delta z}{2})$ $\lvert x'\rvert + \frac{\Delta x}{2} \leqslant \gamma(\lvert z'\rvert + \frac{\Delta z}{2})$	$\frac{1}{2\gamma}\left(\lvert x'\rvert + \frac{\Delta x}{2} - \gamma\left(\lvert z'\rvert - \frac{\Delta z}{2}\right)\right)^2$
8	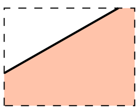	$x' \neq 0, z' \neq 0$ $\lvert x'\rvert - \frac{\Delta x}{2} > \gamma(\lvert z'\rvert - \frac{\Delta z}{2})$ $\lvert x'\rvert + \frac{\Delta x}{2} > \gamma(\lvert z'\rvert + \frac{\Delta z}{2})$	$\Delta x\, \Delta z - \frac{1}{2\gamma}\left(\lvert x'\rvert - \frac{\Delta x}{2} - \gamma\left(\lvert z'\rvert + \frac{\Delta z}{2}\right)\right)^2$
9	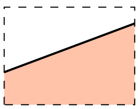	$x' \neq 0, z' \neq 0$ $\lvert x'\rvert - \frac{\Delta x}{2} > \gamma(\lvert z'\rvert - \frac{\Delta z}{2})$ $\lvert x'\rvert + \frac{\Delta x}{2} \leqslant \gamma(\lvert z'\rvert + \frac{\Delta z}{2})$	$\frac{\Delta x}{\gamma}\left(\lvert x'\rvert - \gamma\left(\lvert z'\rvert - \frac{\Delta z}{2}\right)\right)$
10	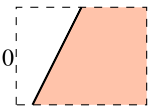	$x' \neq 0, z' \neq 0$ $\lvert x'\rvert - \frac{\Delta x}{2} \leqslant \gamma(\lvert z'\rvert - \frac{\Delta z}{2})$ $\lvert x'\rvert + \frac{\Delta x}{2} > \gamma(\lvert z'\rvert + \frac{\Delta z}{2})$	$\Delta z\left(\lvert x'\rvert + \frac{\Delta x}{2} - \gamma \lvert z'\rvert\right)$

Table 1: Shaded area of each type of singular element centred on $\boldsymbol{x}'$. These thumbnails are shown for quadrant 1; other quadrants are deduced by symmetry. It is helpful to observe that $|x'| = \gamma |z'|$ on the characteristics. In cases 7–10, in addition to the given criteria, we explicitly require that a characteristic passes through the element: in the first and third quadrants, only the η_+ characteristic may intersect the element, but in the second and fourth quadrants, only the η_- characteristic may intersect it. These areas are multiplied by $1/(4\omega^2\gamma)$ to give $\mathrm{Re}\{G_D\}$.

to the right of the wave maker ranging from $z = 0$ to $+\infty$, across which $Q_\omega = 1/(4\omega^2\gamma)$. In both cases, we find that the component of the Green's function flow satisfying the conditions imposed by the physical model of the magic carpet is in phase with the forcing, $\mathrm{Re}\{Q_\omega\}$, and are line jets along the characteristics, which can be represented by δ-functions.

```
Input: $f(\boldsymbol{x}, t)$, $N$
Result: $\chi(\boldsymbol{x}, t)$

$\chi \leftarrow 0$
for $\omega \in \mathbb{R}$ do
    $f_D(\boldsymbol{x}) \leftarrow \frac{\Delta t}{2\pi} \sum_t f(\boldsymbol{x}, t)\, \exp(\mathrm{i}\omega t)$
    // Calculate discrete Green's function using figure 4
    $G_D \leftarrow \mathrm{table}(2N_x - 1, 2N_z - 1)$ // Set up lookup table
    foreach $(i, j) \in G_D$ do
        if Regular element then $G_D(i, j) = $ (3.12)
        else // Singular element
            if $|\omega| > N$ then $G_D(i, j) = $ (3.15)
            else // $|\omega| < N$
                foreach Characteristic do
                    if Element intersection then $\mathrm{Im}\{G_D(i, j)\} = $ (3.17)
                    else $\mathrm{Im}\{G_D(i, j)\} = $ (3.12)
                end
                $\mathrm{Re}\{G_D(i, j)\} = \frac{1}{4\omega^2\gamma} \times$ (shaded area: table 1)
            end
        end
    end

    // Sum over sources according to (3.11)
    $\chi_\omega \leftarrow \mathrm{table}(N_x, N_z)$
    foreach $(k, l) \in \chi_\omega$ do
        $\chi_\omega(k, l) \leftarrow 0$
        foreach $(i, j) \in f_D$ do
            $\chi_\omega(k, l) \leftarrow \chi_\omega(k, l) + G_D(N_x + k - i, N_z + l - j) f_D(i, j)$
        end
    end
    $\chi \leftarrow \chi + \chi_\omega \exp(-\mathrm{i}\omega t)$
end
```

ALGORITHM 1. Calculation of potential χ for an arbitrary source distribution $f(\boldsymbol{x}, t)$. It is calculated mode-by-mode using the discrete monochromatic Green's function, G_D. At each frequency, we first evaluate f_D and G_D, then finally we accumulate contributions to the potential field.

The total volume flux from one finite grid element of width Δx and height Δz that is centred on $(x_0, 0)$ and contains the distribution of monochromatic point sources $f = f_\omega(x, z)\exp(-\mathrm{i}\omega t)$ is

$$\int_{x_0-\Delta x/2}^{x_0+\Delta x/2} \int_{-\Delta z/2}^{\Delta z/2} Q_\omega\, f_\omega(x', z')\exp(-\mathrm{i}\omega t)\,\mathrm{d}z'\,\mathrm{d}x' \approx \Delta x\,\Delta z\,Q_\omega f_\omega(x_0, 0)\exp(-\mathrm{i}\omega t). \tag{4.2}$$

Then, we equate this expression with the corresponding volume flux, $R(t) = R_\omega \exp(-\mathrm{i}\omega t)$, predicted by a physical model of volume displacement by the wave maker surface to obtain the distribution of sources,

$$f_\omega(x_0, 0) = \frac{R_\omega}{\Delta x\,\Delta z\,Q_\omega}. \tag{4.3}$$

For the internal potential, $R_\omega = -\mathrm{i}\omega\Delta x\, h_\omega(x_0)$, so $f_\omega(x_0, 0) = -(2\mathrm{i}\omega/\Delta z)\, h_\omega(x_0)$. Whereas, for the streamfunction, $R_\omega = -(\mathrm{i}\omega\Delta x/2)\, h_\omega(x_0)$, so $f_\omega(x_0, 0) = -\left(2\mathrm{i}\omega^3\gamma/\Delta z\right) h_\omega(x_0)$.

4.2.1. *Internal potential*

For the internal potential, we determine the total vertical volume flux through a line of constant $z \neq 0$,

$$Q(z, t) = Q_\omega(z) \exp(-\mathrm{i}\omega t) = \int_{-\infty}^{\infty} w(x, z, t)\, \mathrm{d}x, \tag{4.4}$$

for the Green's function when $0 < \omega < N$. The vertical velocity field, w, is given by $\partial^3(G_\omega \exp(-\mathrm{i}\omega t))/\partial t^2\, \partial z$ and thus $w = -\omega^2 (\partial G_\omega/\partial z) \exp(-\mathrm{i}\omega t)$. Applying the chain rule to G_ω (3.7) when $z_0 = 0$, we obtain

$$\frac{\partial G_\omega}{\partial z} = -\mathrm{i}\frac{z}{2\pi\omega^2\gamma\left[\left(\frac{x-x_0}{\gamma}\right)^2 - z^2\right]} - \frac{z}{2\omega^2\gamma}\delta\!\left(\left(\frac{x - x_0}{\gamma}\right)^2 - z^2\right). \tag{4.5}$$

Along a path of constant z (where $z \neq 0$) as shown in figure 5, the imaginary part has two simple poles, $x = x_0 \pm \gamma z$, which are where the path crosses the characteristics of G_ω, and $\partial G_\omega/\partial z$ asymptotes inverse-linearly towards them. Between the poles (in the line segment containing $x = x_0$), $\operatorname{sgn}(\mathrm{Im}\{\partial G_\omega/\partial z\}) = +\operatorname{sgn}(z)$, and outside the poles (where $x \to \pm\infty$), $\operatorname{sgn}(\mathrm{Im}\{\partial G_\omega/\partial z\}) = -\operatorname{sgn}(z)$. Thus, we may use the Cauchy principle value to regularise Q_ω at each pole. The imaginary part exhibits even symmetry about $x = x_0$, so it suffices to consider only half of the domain and double the result,

$$\mathrm{Im}\{Q_\omega(z)\} = \lim_{\epsilon\to 0}\left\{\frac{z}{\pi\gamma}\left(\int_{x_0}^{x_0+\gamma z-\epsilon} \frac{\mathrm{d}x}{\left(\frac{x-x_0}{\gamma}\right)^2 - z^2} - \int_{x_0+\gamma z+\epsilon}^{\infty} \frac{\mathrm{d}x}{\left(\frac{x-x_0}{\gamma}\right)^2 - z^2}\right)\right\}. \tag{4.6}$$

Factoring out z^2 and using the substitution $p = (x - x_0)/(\gamma z)$ leaves

$$\mathrm{Im}\{Q_\omega(z)\} = \lim_{\epsilon\to 0}\left\{\frac{1}{\pi}\left(\int_0^{1-\epsilon/(\gamma z)} \frac{\mathrm{d}p}{p^2 - 1} - \int_{1+\epsilon/(\gamma z)}^{\infty} \frac{\mathrm{d}p}{p^2 - 1}\right)\right\}. \tag{4.7}$$

The scaling on the limit variable, ϵ, is the same for both integrals, so we may replace the corresponding limits on the integrals by $1 \mp \epsilon$. Then, evaluating the definite integrals yields

$$\mathrm{Im}\{Q_\omega(z)\} = \lim_{\epsilon\to 0}\left\{\frac{1}{2\pi}\left(\left[\log\frac{1-p}{1+p}\right]_0^{1-\epsilon} - \left[\log\frac{p-1}{p+1}\right]_{1+\epsilon}^{\infty}\right)\right\} = 0. \tag{4.8}$$

Next, we consider the integral over the δ-function in the real part. Along a path of constant z, the argument of the δ-function has two simple zeroes, $y_{1,2} = x_0 \pm \gamma z$, for which we use the standard formula,

$$\delta(f(x)) = \sum_{k=1}^{2} \frac{\delta(x - y_k)}{\left|\frac{\mathrm{d}f}{\mathrm{d}x}\Big|_{y_k}\right|}. \tag{4.9}$$

Here, $\mathrm{d}f/\mathrm{d}x = 2(x - x_0)/\gamma^2$, so we have

$$\mathrm{Re}\{Q_\omega(z)\} = \int_{-\infty}^{\infty} \frac{z}{2\gamma}\left(\frac{\delta(x - [x_0 + \gamma z])}{\left|\frac{2}{\gamma^2}\gamma z\right|} + \frac{\delta(x - [x_0 - \gamma z])}{\left|-\frac{2}{\gamma^2}\gamma z\right|}\right)\mathrm{d}x. \tag{4.10}$$

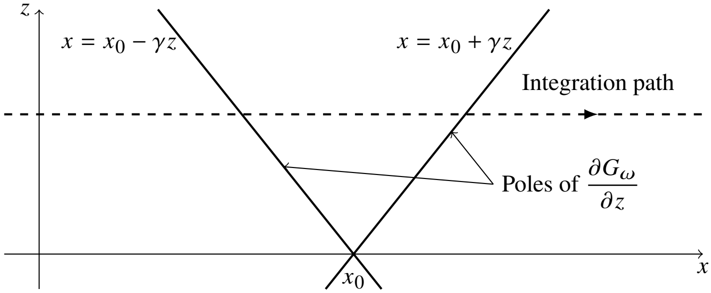

Figure 5: Integration path for calculating the volume flux, Q, for the internal potential, showing the locations of the poles in the imaginary part of $\partial G_\omega/\partial z$, which are also the locations of the singularities in the real part.

Each δ-function contributes a value of one to the integral and $z/|z| = \operatorname{sgn}(z)$, so $\mathrm{Re}\{Q_\omega(z)\} = \frac{1}{2}\operatorname{sgn}(z)$. Therefore, $Q(z) = \frac{1}{2}\operatorname{sgn}(z)\exp(-\mathrm{i}\omega t)$.

The total vertical volume flux through a horizontal transect is half the strength of the internal potential point source and is in phase with the source. The flux has a vertical component everywhere except $z = 0$ and points away from the source when the source is positive. Closing a rectangular contour along $z = \pm z_0$ and $x = \pm\infty$, symmetry arguments determine that the vertical integrals at $x = \pm\infty$ are both zero and integration along the horizontal edges doubles due to the direction in which they are taken. Thus, a monochromatic point source of internal potential of unit strength forces the internal wave equation such that the total volume flux is monochromatic and of unit strength.

We remark that this result also applies to a corresponding integral when the Green's function is for the streamfunction,

$$\int_{-\infty}^{\infty} -u\,\mathrm{d}x = \int_{-\infty}^{\infty} \frac{\partial G_\omega}{\partial z}\,\mathrm{d}x = \frac{1}{2}\operatorname{sgn}(z)\exp(-\mathrm{i}\omega t). \tag{4.11}$$

Using the same rectangular contour, we obtain the circulation around the point source to be $\frac{1}{2}\exp(-\mathrm{i}\omega t)$. Letting $z \to 0$ so that the area enclosed in the contour tends to zero and invoking Stokes' theorem shows that the source is a point vortex of strength $\frac{1}{2}\exp(-\mathrm{i}\omega t)$.

Similar to a resonant simple harmonic oscillator, there are components of the internal potential field both in phase to the forcing and with a phase lag of a quarter oscillation behind the source. Here, the in-phase response ensures the conservation of volume by generating line jets only and exactly along the characteristics, while the phase-lagged response has zero net volume flux despite inducing a flow over the whole domain.

Physically modelling the wave maker, the upwards volume flux generated by an element with vertical displacement h, as shown in figure 6, is

$$R(t) = \int_{x_0-\Delta x/2}^{x_0+\Delta x/2} \frac{\partial h}{\partial t}\,\mathrm{d}x', \tag{4.12}$$

which is approximately equal to $-\mathrm{i}\omega\,\Delta x\, h_\omega \exp(-\mathrm{i}\omega t)$ for small elements. Substituting this into the formula for the required element source strength (4.3) yields the required source strengths for use in the discrete Green's function, $f_\omega(x_0, 0) = -\,(2\mathrm{i}\omega/\Delta z)\,h_\omega(x_0)$.

4.2.2. *Streamfunction*

When the Green's function represents the streamfunction, the volume flux across any horizontal or vertical transect is zero, because sources in the streamfunction internal wave equation are vortices. Instead, since the volume flux across a path is equal to the difference

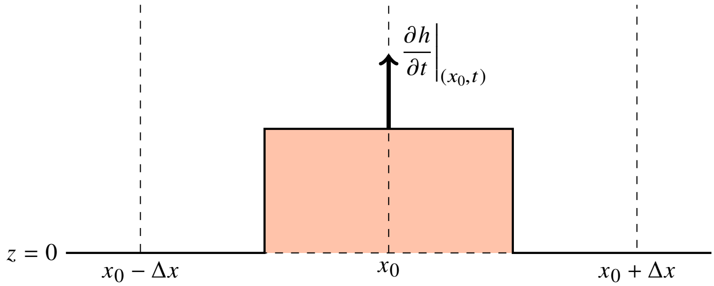

Figure 6: Finite element of width Δx representing wave maker displacement at a single location. We use this model to calculate the induced vertical volume flux required for sources to the internal potential, which is $\Delta x\, \partial h/\partial t|_{(x_0,t)}$. The vertical dashed lines indicate the element centrelines.

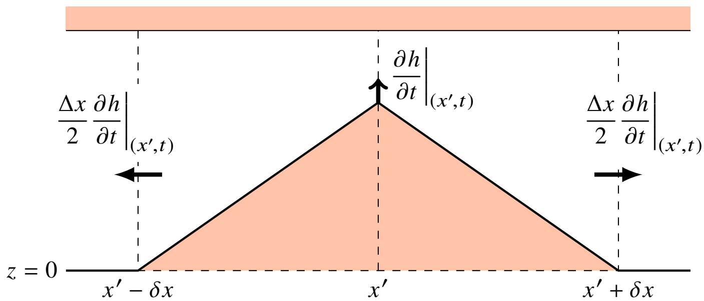

Figure 7: Infinitessimal element representing wave maker displacement at a single location, assuming the profile to be linear between sample points δx apart and the domain to have a rigid lid. We use this model to calculate along-wave maker gradients of induced horizontal volume flux, whose integrals are required for finite sources of width Δx to the streamfunction.

between the values of the streamfunction at each end, we note that the real part of the volume flux induced by G_ω (3.7) across any semi-infinite vertical line from $z = 0$ to $z = \infty$ for constant x is $Q_\omega = 1/(4\omega^2\gamma)$. The point vortex is in phase with the source, so it is not necessary to consider the imaginary part.

For the physical model, we consider a wave maker profile that is spatially sampled every δx and is zero everywhere except at one sample point, $x = x'$, as shown in figure 7. We assume that the wave maker is piecewise linear between the sample points. The rightwards volume flux generated to the right of the displaced infinitesimal element is $R(x' + \delta x, t) = (\Delta x/2)\, \partial h/\partial t|_{(x',t)}$. Conversely, the rightwards volume flux to the left of the element is $R(x' - \delta x, t) = -\,(\Delta x/2)\, \partial h/\partial t|_{(x',t)}$. In the continuum limit, we have

$$\left.\frac{\partial R}{\partial x}\right|_{(x',t)} = \lim_{\delta x \to 0} \frac{R(x' + \delta x, t) - R(x' - \delta x, t)}{2\,\delta x} = \left.\frac{1}{2}\frac{\partial h}{\partial t}\right|_{(x',t)}. \tag{4.13}$$

Integrating such point contributions over a finite element of width Δx centred on $(x_0, 0)$ gives the total horizontal volume flux across one source element,

$$R(x_0, t) = \int_{x_0-\Delta x/2}^{x_0-\Delta x/2} \frac{1}{2}\frac{\partial h}{\partial t}\,\mathrm{d}x \approx \left.\frac{\Delta x}{2}\frac{\partial h}{\partial t}\right|_{(x_0,t)}, \tag{4.14}$$

to leading order in Δx. Thus, $R_\omega = -\,(\mathrm{i}\omega\Delta x/2)\, h_\omega(x_0)$ and $f_\omega(x_0, 0) = -\,(2\mathrm{i}\omega^3\gamma/\Delta z)\, h_\omega(x_0)$.

4.3. *Boundary considerations*

Nonzero-frequency internal waves in a finite domain will inevitably reflect off the top and bottom. In both cases, the fluid cannot flow across the boundary, so we take $w = 0$ as the boundary condition and exploit the characteristic structure of internal waves to enforce it. The required potential, χ, for the reflected wave is calculated along the boundary and then projected along its characteristics using an approach introduced in Dobra *et al.* (2021). The characteristics of the reflected wave are oriented in the opposite vertical, but same horizontal, direction as the incident wave.

For the internal potential in a monochromatic flow, $w = -\omega^2\, \partial\xi/\partial z$ and on the boundary, the reflected wave may take the same value of the internal potential as the incident wave. By contrast, the vertical velocity is obtained from the streamfunction as $w = \partial\psi/\partial x$, giving $\psi =$ const. on the boundary, so we require that the reflected streamfunction is the negative of the incident. In both cases, we set the gauge constant to zero for convenience.

Evaluating χ only on the boundary is insufficient to deduce the horizontal direction of incident characteristics. A wave field of a particular frequency may contain waves in all directions, so we use a principal axes transformation to decompose the incident wave field into left- and right-travelling waves according to the direction of the gradient vector (Dobra 2018, pp. 37–39) and reflect each component in turn.

The interference pattern arising from the distribution of sources generates the desired wave field, but where the source array is abruptly truncated, powerful harmonics are emitted and they may contaminate the solution within the domain. To reduce the severity of such truncation, we smoothly reduce the source strength to zero at the lateral extremities of the calculation domain according to a C^3-continuous ramp that extends well beyond the field of view. Similarly, we use a significantly extended temporal domain for the Fourier transform to avoid periodic reflection in time activity that is aperiodic and short in duration.

4.4. *Experimental method*

The Arbitrary Spectrum Wave Maker (ASWaM, Dobra *et al.* 2019) is a flexible section 1 m long and flush with the base of a tank that is 11 m long, 0.255 m wide and 0.48 m deep. The magic carpet's shape is controlled by an array of 100 linear stepper motors positioned at a pitch of 10 mm, each with a vertical resolution of 0.0127 mm and a stroke of 48 mm.

The surface of the wave maker is a nylon-faced neoprene foam sheet of thickness 3 mm. The material has some resistance to bending, but the attachment mechanism is designed to minimise the tensile stress in the sheet and the bending moments on the actuating rods. We model the surface deformations at each instant, $h(x, t)$, as satisfying

$$\frac{Es^3}{12}\frac{\partial^4 h}{\partial x^4} - T\frac{\partial^2 h}{\partial x^2} = p_*, \tag{4.15}$$

where E is Young's modulus, s is the sheet thickness, T is the longitudinal tension in the sheet and p_* is the pressure difference across the sheet, normally taken as zero. Defining $\lambda = (12T/(Es^3))^{1/2}$, this equation has eigensolutions $\boldsymbol{f}(x) = [1 \quad x \quad \cosh\lambda x \quad \sinh\lambda x]^{\mathrm{T}}$. For our magic carpet, we find that $\lambda \approx 400$. These solutions differ from the typical Euler–Bernoulli linear beam by the presence of hyperbolic functions instead of cubic polynomials, and these differences arise from longitudinal tension. Defining a vector of constants $\boldsymbol{b}$ to be determined by the rod heights and enforcing C^2-continuity, the general solution between each rod is $h(x) = \boldsymbol{b}\cdot\boldsymbol{f}(x)$. Combining the boundary conditions for all sections of the wave maker gives a linear system of equations with constant coefficients, which can be easily inverted numerically.

We fill the tank using the double bucket method (Fortuin 1960; Oster 1965) with a linear density stratification in brine producing a constant buoyancy frequency $N = 1.45\,\mathrm{rad\,s^{-1}}$. We observe density perturbations using Synthetic Schlieren, an optical technique (Dalziel *et al.* 1998; Sutherland *et al.* 1999; Dalziel *et al.* 2000). A static, random pattern of black and white dots is displayed on a 4k (UHD) television screen measuring 1.4 m (55″) on the diagonal that is 0.2 m behind the tank, following Sveen & Dalziel (2005). The light rays emitting from the screen bend as they pass through the varying refractive indices in the tank, and the distorted images are recorded at 4 fps on a 12-megapixel ISVI IC-X12CXP video camera located 3.8 m in front of the tank. A pattern-matching algorithm in the software package DigiFlow (Dalziel Research Partners 2018) is used to reconstruct the gradient of the density perturbation from the recorded images, and we plot its horizontal component, which is related to the internal potential according to $(1/\rho_{00})\,\partial\rho'/\partial x = \left(N^2/g\right)\partial^3\xi/\partial x\,\partial z\,\partial t$.

4.5. *An example: atmospheric lee waves*

A travelling solitary hump is perhaps the simplest aperiodic waveform, directly analogous to flow over an isolated mountain ridge (Dalziel *et al.* 2011). In our experiments, the fluid is stationary in the tank, so boundary layers do not form upstream and we obtain cleaner waveforms.

We seek to validate our numerical model in this configuration, and we choose to calculate the wave field using the internal potential, although we could equally obtain the same wave field using the streamfunction. Our hump consists of a complete wavelength of a sinusoid ranging from trough to trough, where the troughs are flush with the zero height of the magic carpet, with wavelength 0.081 m and peak-to-trough amplitude 0.028 m propagating to the right at $U = 0.0357\,\mathrm{m\,s^{-1}}$. We use 1024 points spanning 50 s for the discrete Fourier transform, giving a frequency resolution of $0.13\,\mathrm{rad\,s^{-1}}$. The hump takes 2.3 s to pass any fixed location, which corresponds to a frequency of $2.8\,\mathrm{rad\,s^{-1}}$. With this adequate temporal resolution, we thus avoid spurious reflections in the time domain.

The passing time of the hump corresponds to a frequency ratio of $\omega/N = 1.88$, which is evanescent. Thus, it is clear that in this case the propagating modes will arise only from peripheral harmonics in the spectrum, an observation to which we will return in §5. Figure 8 compares our experiments with the wave train predicted by our model.

Firstly, from selective withdrawal of modes in our numerical prediction, we deduce that there are significant evanescent modes local to the hump, whose interference pattern is required to capture the structure of the wave train observed in the experiment.

Secondly, we see disturbances spread across the domain, both in front and behind the hump. The waves ahead of the hump appear to be quasi-stationary and persist in the observed timeframe between six and eleven passing periods of the hump after its release. We conclude that these are not simply startup transients, and so we use geometric reasoning to understand the distribution of wave energy in the system.

One common approach is to use the principle of stationary phase (e.g. Lighthill 1978) to restrict our analysis to elements of the wave field that move in phase with the hump. The solitary hump may be characterised as a broadband spectrum of modes all travelling with a common horizontal phase velocity, $\omega/k = U$. It follows that for a given range of wavenumbers, k, there must directly correspond a range of frequencies, ω. Thus, any internal wave propagation generated by the hump has no preferential direction but must share the same horizontal component of phase velocity. The dispersion relation (2.7) constrains the magnitudes of all such wavevectors to the circle $|\boldsymbol{k}| = N/U$. Consequently, for positive frequencies and upwards propagation, only fourth-quadrant wavevectors remain, and their corresponding group velocities point into the first quadrant. These modes comprise the majority of the observed signal, and their superposition results in curved phase lines.

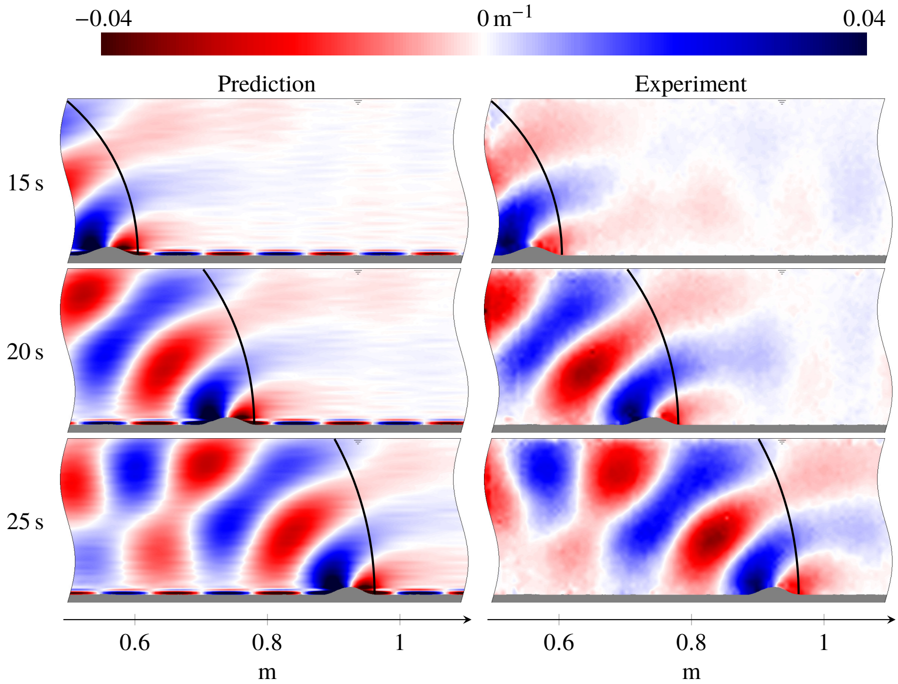

Figure 8: Prediction and experiment comparing $(1/\rho_{00})\,\partial\rho'/\partial x$ for a solitary sinusoidal hump of height 0.028 m and width 0.081 m moving at $U = 0.0357\,\mathrm{m\,s^{-1}}$. Each image is separated by 5 s, and $N = 1.45\,\mathrm{rad\,s^{-1}}$. The majority of the wave energy exists in waves phased-locked with the hump, and these waves are restricted to a semicircular envelope, indicated by the black arc. Wave energy to the right of the arc is carried by non-phase-locked waves, but whose spectrum results in a quasi-steady pattern of waves moving with the hump. There are also evanescent modes forming an interference pattern near the hump, but due to discretisation of the temporal spectrum in our prediction, some leakage of energy occurs along the wave maker surface but the response remains localised.

Furthermore, by following rays traced parallel to each mode's respective group velocity, we may determine a propagation envelope for this class of quasi-steady wave. This envelope forms a semicircle joining the hump's current and initial release locations (Dalziel *et al.* 2011), as shown by black arcs in figure 8. These advancing semicircles grow in radius until the envelope asymptotically forms a vertical front.

Clearly, both the experiment and the prediction contain waves propagating ahead of this envelope, so, as previously noted by Voisin (1994), the principle of stationary phase is insufficient to account for the whole wave field. Given that there is signal high above the wave maker and ahead of the hump, we deduce that these waves must have significant vertical component to their group velocity and therefore have nonzero frequency. Moreover, for internal waves the horizontal component of the group velocity is bounded above by the horizontal component of the phase velocity, and any observable wave ahead of the hump must have group velocity with horizontal component greater than U, so the same must also be true for its phase velocity. Although counterintuitive, it is possible for a composition of modes from a spectrum of phase velocities to form a quasi-steady wave field that translates with a single apparent phase velocity. Akin to the decomposition of a standing wave into opposing travelling waves, a carefully chosen difference of frequencies is sufficient to create the required behaviour, although many combinations of wavevector and frequency would

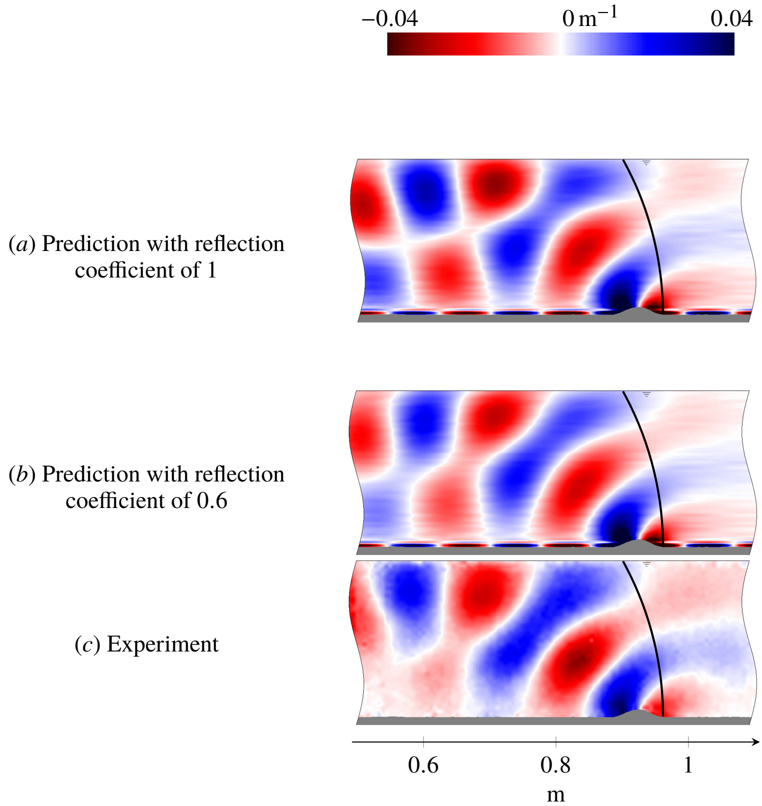

Figure 9: Predictions assuming pure reflections (*a*) and with calibrated attenuation at the free surface with coefficient 0.6 (*b*) compared to experiment (*c*). These correspond to figure 8 at 25 s and show $(1/\rho_{00})\,\partial\rho'/\partial x$. Without attenuation, the predicted amplitude of the wave field behind the hump is larger than observed. The reflection coefficient accounts for energy dissipated at the free surface through mechanisms not directly modelled.

also produce an equivalent result. We conjecture that just such a superposition of modes is responsible for propagation ahead of the envelope shown in figure 8.

We note that our approach requires the Fourier transform in time of the entire timeline. Since the source strengths are zero at all times except when the hump is passing, the ω-spectrum is broad. However, a discrete Fourier transform introduces discretisation error, which when inverted produces sources at unwanted times. We see their effect as forced oscillations along the magic carpet, which have insignificant effect on the rest of the wave field.

Our wave propagation model does not directly account for energy leaving the modelled system during a reflection, yet is present in the experiments. We employed a line-search optimisation to determine suitable calibration parameters and accordingly modify the reflections at the free top surface by 0.6 while maintaining pure reflections at the solid bottom boundary. Figure 9 demonstrates the necessity of accounting for this energy loss.

5. Interactions of finite-width internal wave beams

5.1. *Introduction*

The literature on internal wave laboratory experiments can be divided into two broad lines of enquiry: work following from Görtler (1943) and Mowbray & Rarity (1967) on waves generated by a small oscillating body, and work on quasi-monochromatic line sources following McEwan (1971, 1973). The capability of our magic carpet allows us to span the range between these limiting cases, and although previous work using it (Dobra *et al.* 2021) validated new theoretical predictions in the line-source limit, we seek here to demonstrate the generality of these findings by applying them to an intermediate regime. We examine the interactions of finite-width wave beams a few wavelengths across, since recent explorations of such configurations (Smith & Crockett 2014) have uncovered a rich dynamical structure. We have unparalleled access to observe and analyse such wave fields processed first with Synthetic Schlieren and then with Dynamic Mode Decomposition (DMD, Schmid 2010). For the cases we consider here, DMD is an ideal tool because the frequency discretisation is responsive to the input, so it takes many fewer samples to accurately recover the dominant frequencies compared with Fourier methods which project onto basis functions at a fixed discretisation. Furthermore, DMD enables us to distinguish between steady-state behaviours and transient modes. Our experiments have been carefully configured so that steady-state behaviours dominate, and we do not observe the common unsteady phenomenon of triadic resonant instability.

5.2. *A series expansion for triadic interactions*

Building on the recent developments of Dobra *et al.* (2021), here we introduce a fusion of our perturbation expansion framework and the method of solution by Green's function, enabling us to construct general wave fields from the interference patterns produced by a distribution of sources. In Dobra *et al.*, the perturbation expansion at each order yields the internal wave equation in terms of the streamfunction with sources that are Jacobian determinants. Under particular symmetries, we found that these sources cancel, preventing a broad class of wave–wave interactions from occurring. Here, we instead consider configurations where these sources play a significant role in the structure of the wave field, and employing the Green's function with the streamfunction potential, it integrates naturally. We now outline a generalisation of our perturbation framework for these arbitrary wave fields.

We reformulate the conservation of momentum (2.1) and mass (2.3) in terms of streamfunction, ψ, and buoyancy, $b = -g\rho'/\rho_{00}$,

$$\frac{\partial}{\partial t}\nabla^2\psi + \left|\frac{\partial\left(\psi, \nabla^2\psi\right)}{\partial(x,z)}\right| = \frac{\partial b}{\partial x}, \tag{5.1a}$$

$$\frac{\partial b}{\partial t} + \left|\frac{\partial(\psi, b)}{\partial(x,z)}\right| = -N^2\frac{\partial\psi}{\partial x}, \tag{5.1b}$$

where the Jacobian determinant of two scalars, α and β, is given by

$$\left|\frac{\partial(\alpha,\beta)}{\partial(x,z)}\right| = \frac{\partial\alpha}{\partial x}\frac{\partial\beta}{\partial z} - \frac{\partial\alpha}{\partial z}\frac{\partial\beta}{\partial x}. \tag{5.2}$$

Eliminating the linear b terms leaves the nonlinear internal wave equation,

$$\frac{\partial^2}{\partial t^2}\nabla^2\psi + N^2\frac{\partial^2\psi}{\partial x^2} = \frac{\partial}{\partial t}\left|\frac{\partial\left(\nabla^2\psi, \psi\right)}{\partial(x,z)}\right| + \frac{\partial}{\partial x}\left|\frac{\partial(b,\psi)}{\partial(x,z)}\right|. \tag{5.3}$$

Nonlinearity associated with triadic interactions is captured by source terms of the form of Jacobian determinants, and here we consider their behaviour in the case

$$\psi = \sum_{j=1}^{3} \left\{ A_j \exp\left(\mathrm{i}\left[\boldsymbol{k}_j \cdot \boldsymbol{x} - \omega_j t\right]\right) + A_j^* \exp\left(-\mathrm{i}\left[\boldsymbol{k}_j \cdot \boldsymbol{x} - \omega_j t\right]\right) \right\}, \tag{5.4}$$

where we require complex conjugate (*) pairs to represent real wave fields. The source terms multiply pairs of waves, so we must consider each possible pairing in turn. Self interactions equate to zero (McEwan 1973; Tabaei & Akylas 2003; Dobra *et al.* 2021), but the interaction of beam $j = 1$ with beam $j = 2$ produces terms proportional to $\exp(\mathrm{i}[(\boldsymbol{k}_2 + \boldsymbol{k}_1) \cdot \boldsymbol{x} - (\omega_2 + \omega_1)t])$ and $\exp(\mathrm{i}[(\boldsymbol{k}_2 - \boldsymbol{k}_1) \cdot \boldsymbol{x} - (\omega_2 - \omega_1)t])$ and their complex conjugates. Thus, by index manipulation we may define

$$\boldsymbol{k}_3 = \boldsymbol{k}_2 \pm \boldsymbol{k}_1, \tag{5.5a}$$

$$\omega_3 = \omega_2 \pm \omega_1. \tag{5.5b}$$

Should this disturbance characterised by $\boldsymbol{k}_3$ and ω_3 satisfy the dispersion relation (2.7), $\omega_3 = N k_3/|\boldsymbol{k}_3|$, the disturbance is also a wave and the source terms are an eigensolution of the internal wave equation (2.9). Such combinations are commonly described as resonant triads.

We examine in figure 10(a) the geometric permutations of wave triad that may be constructed for a given $\boldsymbol{k}_1$, ω_1 and fixed frequency ω_2 but where wavevector $\boldsymbol{k}_2$ is unconstrained. These triangles are compatible with the selection rules derived by Tabaei *et al.* (2005) and Jiang & Marcus (2009) that determine into which quadrants, if any, a new wave beam may be emitted. These configurations are typical of wave beams a few wavelengths across for which the wavenumber spectra are broad. In these cases, the spectrum of the source terms is significant across a patch of wavevector space, as shown in figure 10(b). Wavevectors that lie on the dashed locus of dispersion-relation-satisfying $\boldsymbol{k}_3$ will resonate, and new waves will emerge by mode selection; these correspond to cases where the triangle of wavevectors can be closed.

No polychromatic solutions containing multiple horizontal phase velocities are known for the fully nonlinear equation (5.3), so in Dobra *et al.* (2021), we performed a perturbation expansion to give a recursive algorithm that we can truncate at finite order to calculate an approximate solution. In this earlier work, we expanded ψ in powers of a small parameter, a, which we took to be the wave steepness. Instead, here we modify the expansion to be $\psi = \sum_{n=1}^{\infty} \psi_n$, where each subsequent term drops an order of magnitude, and the expansion for b behaves correspondingly. Then, as our earlier work showed, each order satisfies

$$\frac{\partial^2}{\partial t^2}\nabla^2\psi_n + N^2\frac{\partial^2\psi_n}{\partial x^2} = \sum_{p=1}^{n-1}\left\{\frac{\partial}{\partial t}\left|\frac{\partial\left(\nabla^2\psi_p, \psi_{n-p}\right)}{\partial(x,z)}\right| + \frac{\partial}{\partial x}\left|\frac{\partial\left(b_p, \psi_{n-p}\right)}{\partial(x,z)}\right|\right\}. \tag{5.6}$$

There is a cascade of information from lower order to higher, but not in reverse, thus the expansion is purely inductive. However, at all orders greater than three, there are contributions to frequencies that already exist at lower orders. There is an infinite series of such contributions to the wave field, some of which manifest as corrections to existing wave beams (as we will see later in figure 14) but may also generate waves propagating in new directions. We use the polarisation relation of linear internal waves to calculate $b = N^2 \int \partial\psi/\partial x \, \mathrm{d}t$.

5.3. *Computational method*

We use a method based on integration across finite elements to predict the steady-state wave field due to two crossing internal wave beams, exploiting the symmetry of the complex

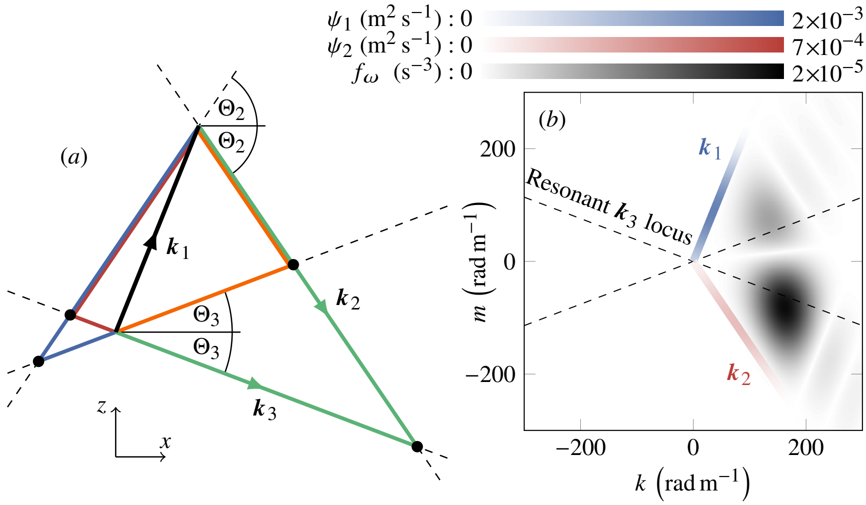

Figure 10: Wavevector triangles for the sum of frequencies $\omega_1 + \omega_2$ in the case $\omega_1 = 0.55\,\mathrm{rad\,s^{-1}} = 0.37N$ and $\omega_2 = 1.5\omega_1$. In (*a*), all permutations of wavevector triangles are presented for the case where $\boldsymbol{k}_1$ points into the first quadrant. The triangles for all other quadrants are obtained by reflective symmetry. From the dispersion relation (2.7), each frequency has four possible directions for its wavevector, one in each quadrant. Given $\boldsymbol{k}_1$, the loci of $\boldsymbol{k}_2$ and $\boldsymbol{k}_3$ will in general close to form a triangle in one of four different ways. A closed triangle is a resonant triad. In (*b*), we plot in greyscale the distribution of source term amplitudes in Fourier space for incident wavevector distributions $\boldsymbol{k}_1$ (blue) and $\boldsymbol{k}_2$ (red). The resonant, propagating $\boldsymbol{k}_3$ lie at the intersections of each of the dashed lines with regions of significant source amplitude. The remainder produce a local interference pattern of forced oscillations. In this configuration, two waves at ω_3 are emitted: a weaker one with $\boldsymbol{k}_3$ pointing into the first quadrant (wave propagating down and to the right, triangle marked in orange in (*a*)), and a stronger one with $\boldsymbol{k}_3$ pointing into the fourth quadrant (up and to the right, green triangle in (*a*)).

conjugate to avoid unnecessary execution. In the general case, we use a calculation domain of 346×57 elements with aspect ratio one, and incident waves are produced using an array of sources, following the method in §4. For these configurations, we plot $(1/\rho_{00})\,\partial\rho'/\partial z = \left(N^2/g\right)\int\left(\partial^2\psi/\partial x\,\partial z\right)\mathrm{d}t$.

The source terms to the internal wave equation involve third-order derivatives, and any errors may propagate across the domain in spurious wave beams. These derivatives are recursively applied each time we increase the order of the perturbation expansion. In our calculations, we evaluate the expansion to third order and thus the original field is differentiated six times. To control numerical noise, we use ghost cells to employ eighth-order centred finite differences, and we perform one sweep of elliptic smoothing to eliminate mesh-scale truncation error in these derivatives. We take care to ensure that there is a separation of length scale between those of the input and those associated with the mesh, thus the smoothing has negligible effect on derivatives that contribute to the physics of the system.

Where we look at the detailed physics of wave-wave interactions, we initialise the streamfunction with idealised waveforms corresponding to magic carpet displacement profiles,

$$h = A\exp\left(\mathrm{i}[kx - \omega t]\right)\cos^3\left(\frac{\pi}{L}x\right)\mathrm{H}\left(\frac{L}{2} - |x|\right). \tag{5.7}$$

The amplitude of the wave, A, and the width of the envelope, L, are configured to match the experiments, which themselves are configured to approximate the asymptotic limit of a wave beam propagating in a viscous fluid (Hurley & Keady 1997; Sutherland *et al.* 1999). However, such waveforms have a broad spectrum including both left- and right-travelling waves (see Dobra *et al.* 2019). To produce a unidirectional wave, we nullify Fourier modes according to their sign and transform back into physical space, a procedure known as the Hilbert transform (Mercier *et al.* 2008). Then, we project this profile along the characteristics, using cubic spline interpolation to obtain element-centred values. For these calculations, we use a grid of 128×128 elements with aspect ratio that are non-unity.

5.4. *Experimental method*

We use the same experimental apparatus and diagnostics as §4. To maximise the amplitudes of the wave beams without inducing locally separated flow near the magic carpet, the amplitudes are increased linearly from rest before reaching a steady state. Data acquisition is performed over two minutes in this steady state. To build on the work of Tabaei *et al.* (2005), Jiang & Marcus (2009) and Smith & Crockett (2014), we seek to examine multiple orientations of incident wave beams and achieve these by exploiting reflections off the free surface, as shown in figure 11(a).

Here, we use the technique of Dynamic Mode Decomposition (DMD, Schmid 2010) to identify the temporal modes of a video sequence. Closely related to proper orthogonal decomposition, the method takes an observable representation of the system's state, $\boldsymbol{y}$, and finds the best-fit system evolution operator, $\boldsymbol{A}$, such that $\mathrm{d}\boldsymbol{y}/\mathrm{d}t = \boldsymbol{A}\boldsymbol{y}$ when averaged over some period. If $\boldsymbol{Y}$ is composed of a temporal sequence of column vectors of states $\boldsymbol{y}$ and we let $\boldsymbol{Y} = \boldsymbol{U}\Sigma\boldsymbol{V}^{\mathrm{T}}$ be its singular value decomposition, then $\hat{\boldsymbol{U}}$ may denote a truncation of $\boldsymbol{U}$ that only includes modes with important singular values. Performing an approximate principal axis transformation of $\boldsymbol{A}$ to the truncated basis $\hat{\boldsymbol{U}}$ and then an eigendecomposition of $\boldsymbol{A}$ in the new basis, we have

$$\boldsymbol{A} \approx \hat{\boldsymbol{U}}\hat{\boldsymbol{A}}\hat{\boldsymbol{U}}^{\mathrm{T}} = \hat{\boldsymbol{U}}\hat{\boldsymbol{W}}\hat{\Lambda}\hat{\boldsymbol{W}}^{-1}\hat{\boldsymbol{U}}^{\mathrm{T}}. \tag{5.8}$$

The dynamic modes are the pairing $\hat{\boldsymbol{U}}\hat{\boldsymbol{W}}$, and generally they each have distinct complex conjugate pairs of eigenvalues, whose phases determine their frequencies. They may be independently evolved in time, but here we plot these modes evaluated at a common time origin.

5.5. *Results and discussion*

We begin by comparing our numerical prediction with the output of the Synthetic Schlieren in figure 11 using parameters as given in table 2. We highlight each visible wave beam schematically in figure 11(c) using the colours blue, red, green and orange to indicate successive orders of the perturbation expansion in §5.2. Our priority is to examine wave–wave interactions, and while there are many in this figure, the principal interaction zone is outlined by the grey box. Since this will be our region of focus for subsequent results, we take care to optimise the wave field geometry for diagnostic quality in this region. For our prediction to match well, we account for experimental artefacts such as weak viscous spreading of wave beams and some unavoidable curvature in the stratification near the top and bottom boundaries, so we make small perturbations to waves generated on the synthetic wave maker to ensure that waves incident to the boxed region have beam widths and amplitudes that match the experiment. Given comprehensive frequency-decomposed post-processing of experiments, we are able to perform a thorough calibration of the transmission efficiency from order to order. We find by line-search optimisation that it takes a globally constant

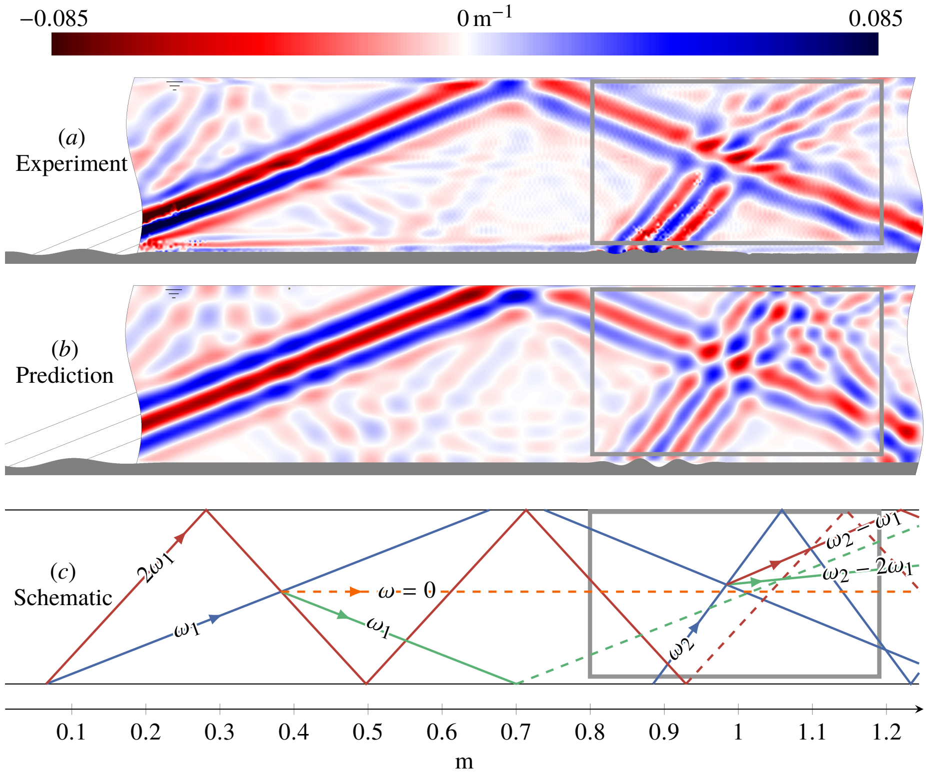

Figure 11: Geometry of wave beams in tank for intersecting two internal waves with the same horizontal direction and opposite vertical direction of the group velocity. Subfigure (a) shows our experiment, subfigure (b) shows our corresponding prediction, and subfigure (c) shows a schematic of all visible wave beams with blue, red, green and orange corresponding to first-, second-, third- and fourth-order waves respectively. Beam 1, of frequency $\omega_1 = 0.55\,\mathrm{rad\,s^{-1}} \approx 0.37N$, is generated at the left end of the wave maker, then reflects off the free surface to intersect beam 2, of frequency $\omega_2 = 2.2\omega_1$. Among others, a triadic interaction generates a third wave beam at frequency $\omega_2 - \omega_1$ in the grey rectangle, which is the region of interest in subsequent figures. The diagnostic shown is the vertical gradient of the normalised density perturbation, $(1/\rho_{00})\,\partial\rho'/\partial z$.

value of $\sim \frac{1}{2}$ across all interactions and all experiments. It remains an open question why the perturbation expansion requires such order-to-order calibration, but by matching our hierarchical decomposition with suitably post-processed experiments, we have identified a discrepancy that could not have been anticipated in advance.

In the primary interaction zone, two significant new waves are emitted up and to the right: one at second order (shown in red in figure 11(c)) of frequency $\omega_2 - \omega_1$ due to the interaction of beam 2 with beam 1, and the other at third order (shown in green) of frequency $\omega_2 - 2\omega_1$ due to the interaction of the first additional wave with beam 2. Where the reflections of both beams 1 and 2 intersect, we note an interference pattern leads to a distortion of the phase lines in the bottom-right corner of the grey box.

The left end of the magic carpet, just outside our diagnostic field of view in the experiment (and replicated in the numerical prediction), also emits a second harmonic for beam 1, which reflects off the free surface before interacting with its fundamental beam. From this interaction, an additional wave of frequency ω_1 (shown in green in figure 11(c)) is emitted though here its direction is down and to the right. This beam reflects off the bottom boundary

Figure	11	12	13	14	15
N (rad s^{-1})	1.50	1.47	1.47	1.41	1.48
ω_1 (rad s^{-1})	0.55	0.55	0.55	0.4	0.8
k_1 (rad m^{-1})	39	26	36	48	80
A_1 (mm)	2.8	1.8	1.4	1.8	2.6
L_1 (m)	0.42	0.34	0.25	0.30	0.12
ω_2 (rad s^{-1})	1.21	1.21	0.825	1.2	1.2
k_2 (rad m^{-1})	121	110	75	−40	100
A_2 (mm)	1.8	1.7	1.4	4.2	2.4
L_2 (m)	0.26	0.18	0.15	0.14	0.11

Table 2: Parameters for each configuration considered, as defined by (5.7).

and also happens to intersect the primary interaction zone. Since the second harmonic is present only at second order (Dobra *et al.* 2021), this additional ω_1 beam is third-order, so for a prediction truncated at third order, we do not include any of its interactions with other wave beams. Also visible in the experiment is a fourth-order zero-frequency wave (shown in orange) arising from the interaction of the first- and third-order waves of frequency ω_1. While strictly zero-frequency modes cannot propagate, in the asymptotic limit, they closely resemble gravity currents generated by transient irreversible displacement of mass. Indeed, these also form near the bottom boundary, and we attribute this small aberration to boundary-layer mixing.

On its third reflection, the second harmonic of ω_1 intersects its fundamental once more, this time just after its own reflection off the free surface. We calibrate the strength of reflections in our predictions to account for surface wave transmission away from reflection sites, and we find an absorption coefficient of 30 %. Furthermore, evaporative cooling acts to smooth the top interface, which in turn creates complex reflection geometries; we account for these by applying a phase shift and a higher absorption coefficient of 55 % to beam 1 only.

In figure 12 for a similar configuration, we expand out all the wave contributions at each order and frequency, and compare with the DMD of the experiment. We restrict the viewing window to the grey box in figure 11. The first row contains the superposition of all the wave beams at each order of truncation. At first order, there are no interactions, so we have only the linear superposition of incident waves. At second order, we obtain by triadic interactions a new pair of frequencies, $\omega_2 - \omega_1$ and $\omega_2 + \omega_1$.

Eight triads are possible at third order, formed from each combination of a first-order and a second-order wave, and in each combination both difference and sum of frequencies may emerge. Four of these triads produce new frequencies, meanwhile there is a pair of triads from which will emerge new contributions to ω_1 and a corresponding pair for ω_2. The triads for ω_1 are $-(\omega_2 - \omega_1) + \omega_2$ and $(\omega_2 + \omega_1) - \omega_2$, and for ω_2, they are $(\omega_2 - \omega_1) + \omega_1$ and $(\omega_2 + \omega_1) - \omega_1$. For the configuration in this figure, these contributions are present but very weak and must not be confused with the third-order ω_1 wave in the bottom-left that, similarly to figure 11, arises from the interaction of $2\omega_1$ and ω_1 well to the left of the viewing window; we verified the wave direction in the experiment using the Hilbert transform. We also note that at third order, there are neither contributions to $\omega_2 - \omega_1$ nor $\omega_2 + \omega_1$; such additional contributions only appear from fourth order onwards.

Of the new frequencies generated at third order, only $\omega_2 - 2\omega_1$ has appreciable amplitude. This propagating wave bends on the boundary of the interaction zone, because dominant

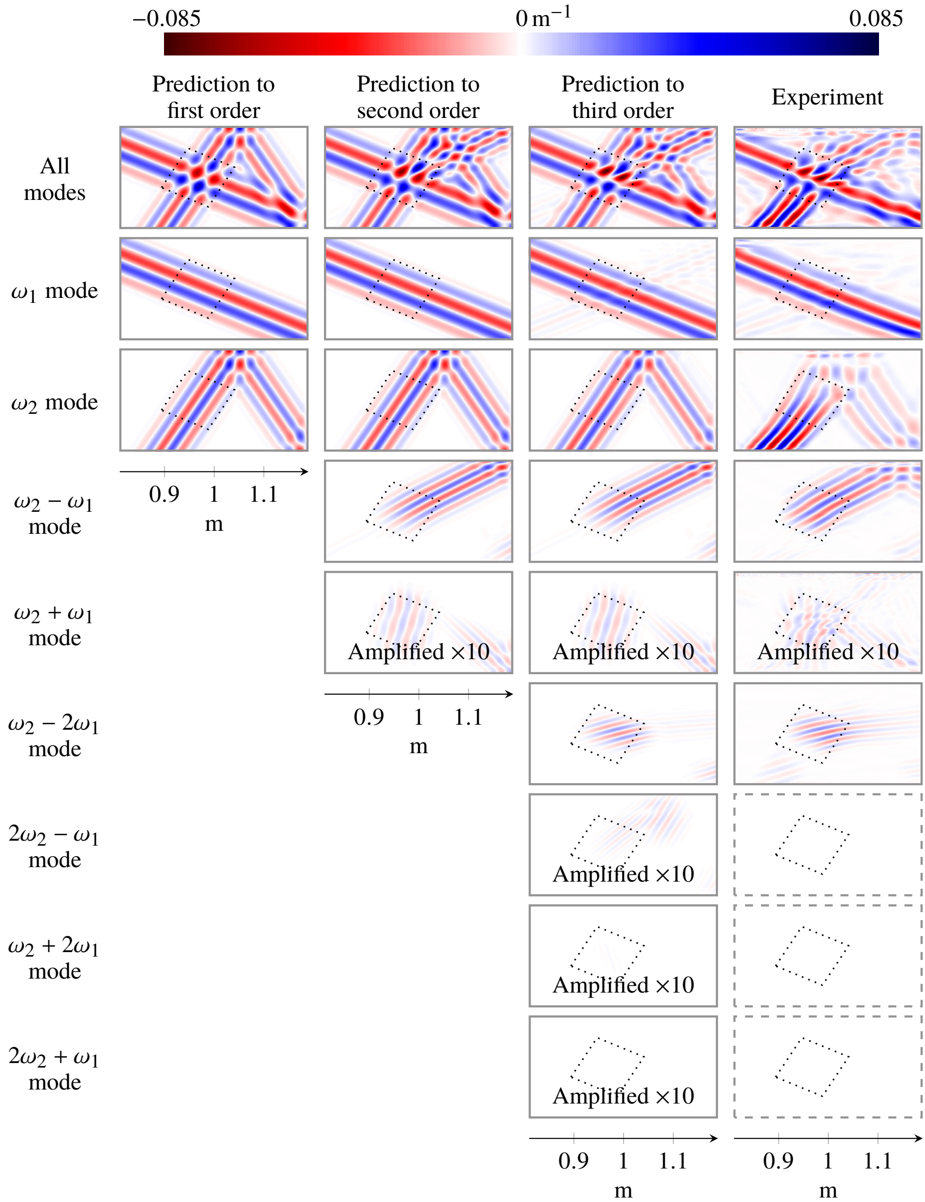

Figure 12: Hierarchical decomposition of the internal wave field where $\omega_1 \approx 0.37N$ and $\omega_2 = 2.2\omega_1$. We plot the real part of evolutionary modes of the diagnostic, $(1/\rho_{00})\,\partial\rho'/\partial z$, and for reference mark the parallelogram where the incident waves cross with dotted lines. At first order in the expansion, we only obtain the incident waves. At second order, we obtain $\omega_2 - \omega_1$ and $\omega_2 + \omega_1$. At third order, we not only obtain four new frequencies, but we obtain new contributions to ω_1 and ω_2 that in this configuration are small in amplitude but broaden the wave beams. There are no further contributions to $\omega_2 - \omega_1$ and $\omega_2 + \omega_1$ until fourth order. The final column compares with DMD, and the dashed grey boxes indicate where experimental noise obscured the frequency from detection. We do not constrain the DMD to deliver prescribed frequencies; the best-fit modes are always returned.

wavevectors in the source terms do not satisfy the dispersion relation so the associated modes are confined as forced oscillations, meanwhile the slightly weaker resonant modes are preferentially selected and propagate away from the interaction zone. We also note other artefacts visible in both the experiment and the prediction at this frequency. The other three new frequencies are evanescent and are too weak to have significant singular values when computing the DMD, so we represent these missing modes by boxes with dashed borders.

As noted by Bourget *et al.* (2014), the amplitudes of new propagating waves, such as $\omega_2 - \omega_1$, grow linearly across the interaction zone where the source terms are large. Outside this zone, propagating over an area with insignificant sources, they have approximately constant amplitude. Conversely, forced oscillations have amplitudes that are proportional to the local source terms. In this example, $\omega_2 + \omega_1 > N$ and produces weak evanescent modes that decay exponentially with distance from the interaction zone, so we amplify its images by a factor of ten. We see a second generation zone of this mode where the reflection of ω_2 intersects ω_1 again in the bottom-right of the domain.

Figure 13 is similar to the previous two cases, but configured such that $\omega_2 + \omega_1 < N$. This mode is emitted to the right both upwards and downwards, but the upwards-propagating mode is stronger and noticeably reflects several times within our field of view, thus the configuration is dense with opportunities for third-order interactions in the right half of the image. One such interaction is the broad addition to ω_2 in the bottom-right corner, and there is a corresponding beam at ω_1 in the top-right corner.

Due to our choice here of $\omega_2 = 1.5\omega_1$, some frequencies are duplicated by multiple modes. In particular, $|\omega_2 - 2\omega_1| = \omega_2 - \omega_1$, but geometrically the wavevectors cannot organise to form a contribution from $\omega_2 - 2\omega_1$, consistent with the selection rules of Tabaei *et al.* (2005) and Jiang & Marcus (2009). In addition, a reflection of the second harmonic of beam 1 passes close to the interaction zone, and its interaction with beam 2 near the left vertex of the main interaction zone also produces two waves at $\omega_2 - \omega_1$, which propagate in each of the downward directions. Although the dominant components of $2\omega_1$ and ω_1 have a common horizontal phase velocity and thus have a symmetry that prevents them from interacting (Dobra *et al.* 2021), each wave beam is monochromatic in frequency but has a broad wavenumber spectrum, so provided we satisfy the geometric selection rules, a full spectrum of resonant modes will still be generated. Moreover, $2\omega_1$ has third-order interactions with ω_1 and ω_2, but the only appreciable contribution is $2\omega_1 + \omega_1 = 3\omega_1$. One component of this signal is a weak evanescent second harmonic of beam 2, visible in the bottom-left corner, and appears here because $2\omega_2 = 3\omega_1$ by construction. However, the dominant signal in the DMD mode at $3\omega_1$ is a forced oscillation associated with beam 2, and we do not consider this mechanism in our model, so a direct comparison cannot easily be drawn.

In numerous places, our experiment demonstrates the presence of yet higher-order interactions. Firstly, in the bottom-right corner of the $\omega_2 - \omega_1$ panel, there is a broadening of this wave beam that appears analogous to the previously noted third-order contributions to ω_1 and ω_2. This contribution may be generated by a fourth-order interaction between ω_1 and the $\omega_2 - \omega_1$ component that is itself generated by the second harmonic, $2\omega_1$, and its fundamental, ω_1. Secondly, the DMD at $2\omega_2 - \omega_1$ exhibits waves originating in the main interaction zone. We do not predict them at third order, but do expect to find them at higher orders. Although our prediction of their amplitudes is poor, we do capture elements of their structure. We also note that in the top-right corner, we have successfully predicted the third-order interaction $(\omega_2 - \omega_1) + \omega_2$.

In the following figures, we select some interesting alternative geometries. Figure 14 considers the interaction of left- and right-running waves, and figure 15 considers incident waves from the same quadrant that interact obliquely.

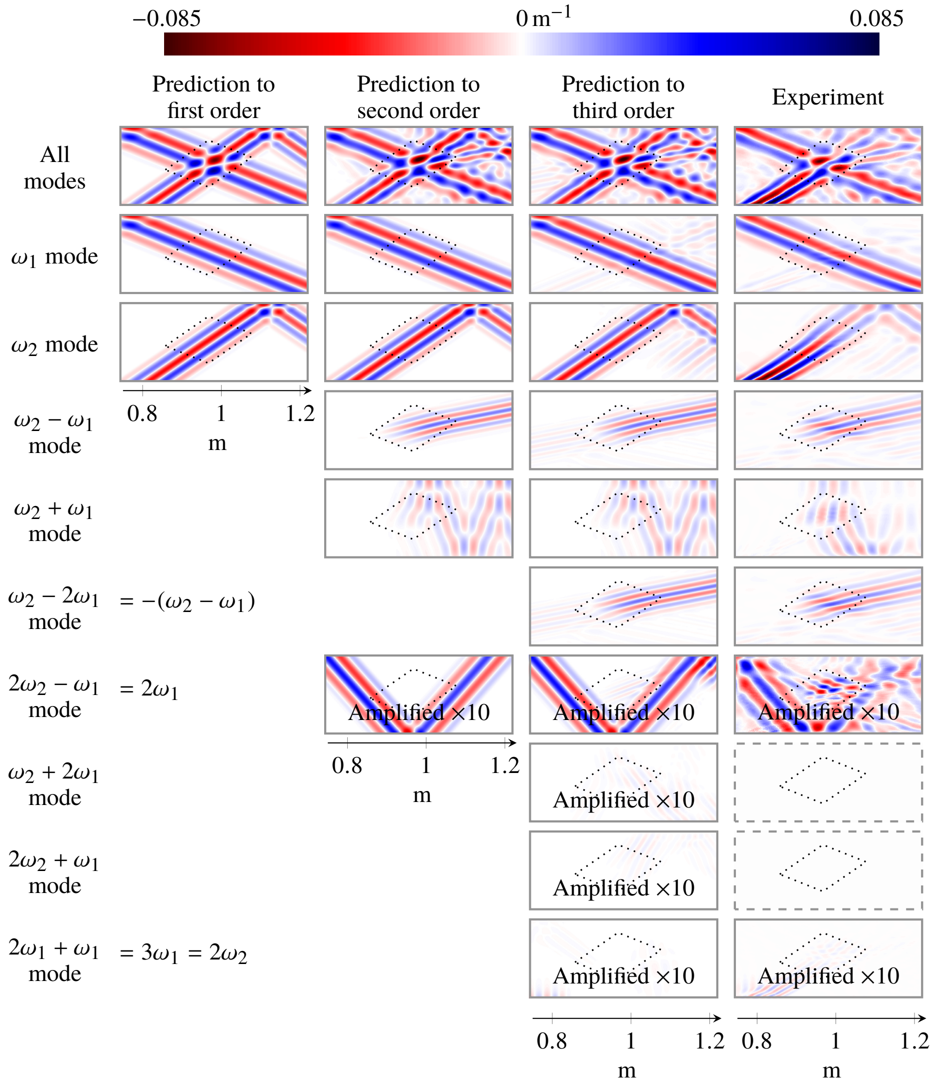

Figure 13: Hierarchical decomposition of the internal wave field where $\omega_1 \approx 0.37N$ and $\omega_2 = 1.5\omega_1$. We plot the real part of evolutionary modes of the diagnostic, $(1/\rho_{00})\,\partial\rho'/\partial z$, and for reference mark the parallelogram where the incident waves cross with dotted lines. Here, $\omega_2 + \omega_1 < N$, so new waves can be emitted. This corresponds to the geometry presented in figure 10, and we see that these waves are emitted in two directions. In this case, several frequencies are duplicated by contributions from multiple sources; in particular, $|\omega_2 - 2\omega_1| = |\omega_2 - \omega_1|$. Other duplicates arise from the second harmonic of beam 1, which first appears at second order and just misses the main interaction zone. The final column compares with DMD, and the dashed grey boxes indicate where experimental noise obscured the frequency from detection.

With waves in opposite horizontal directions, we have the opportunity to maximise the interaction strength by choice of frequencies. The source terms arise from the $\boldsymbol{u}\cdot\boldsymbol{\nabla}$ advection operators in the governing equations (2.1) and (2.3). The velocity, $\boldsymbol{u}$, points along the wave beam, meanwhile all gradients are perpendicular to the beam. In the case where the two beams are orthogonal, $\boldsymbol{u}$ of one beam is aligned with the gradient vector of the other, and thus the

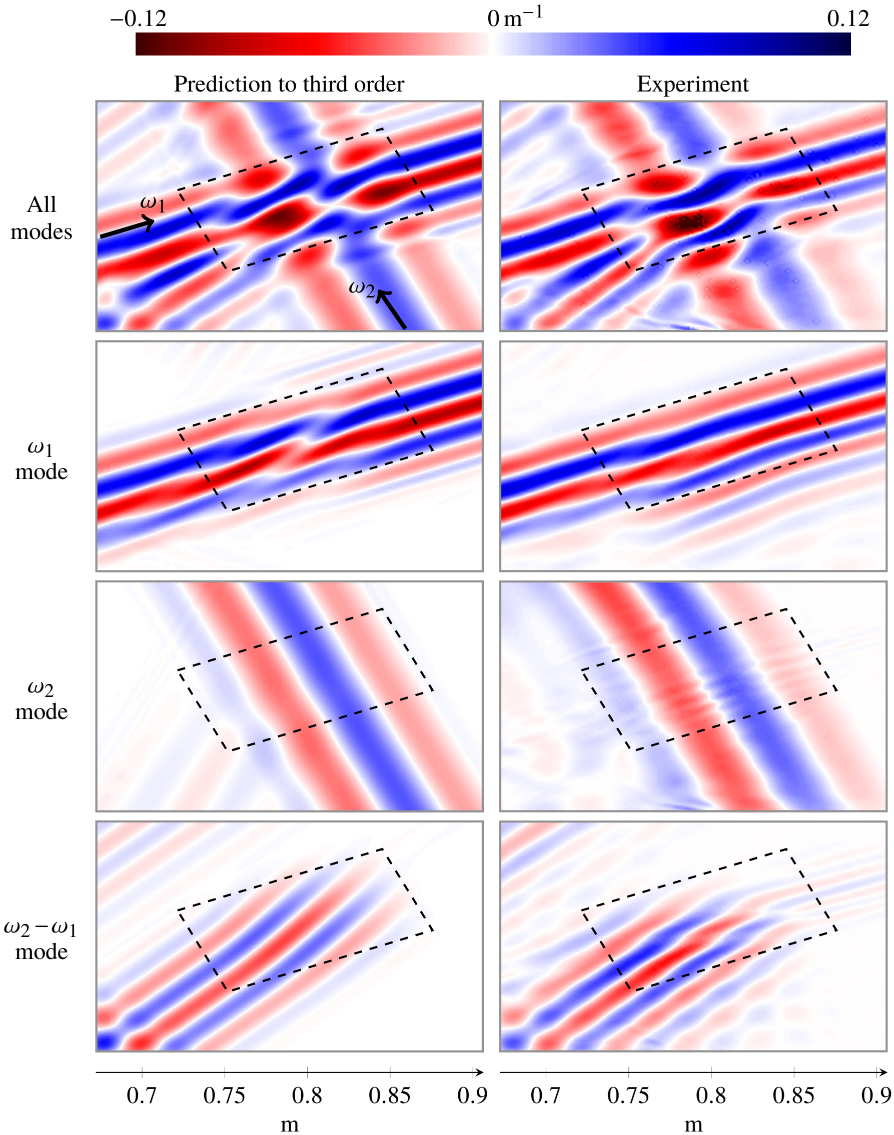

Figure 14: Decomposition of the internal wave field where $\omega_1 \approx 0.28N$ and $\omega_2 = 3\omega_1$. We plot the real part of evolutionary modes of the diagnostic, $(1/\rho_{00})\,\partial\rho'/\partial z$, and for reference mark the parallelogram where the incident waves cross with dotted lines. We notice in particular distortion of phase lines of ω_1 due to third-order contributions. For completeness, we include the second harmonic of ω_1, since this has the same frequency as $\omega_2 - \omega_1$.

source terms will be maximal. In figure 14, we demonstrate a near-orthogonal configuration with the additional property that the dominant $\boldsymbol{k}_2 - \boldsymbol{k}_1$ is near-resonant.

Due to these strong interactions at second order, we have a clear view of the third-order contributions to ω_1. These broaden the beam significantly, introduce a distortion of the phase and slightly increase the amplitude. In addition, the second harmonic of beam 1 has frequency $\omega_2 - \omega_1$ and appears in the top-left corner, which interacts with its fundamental beam to produce third-order forced oscillations at ω_1 whose wavevectors do not align with

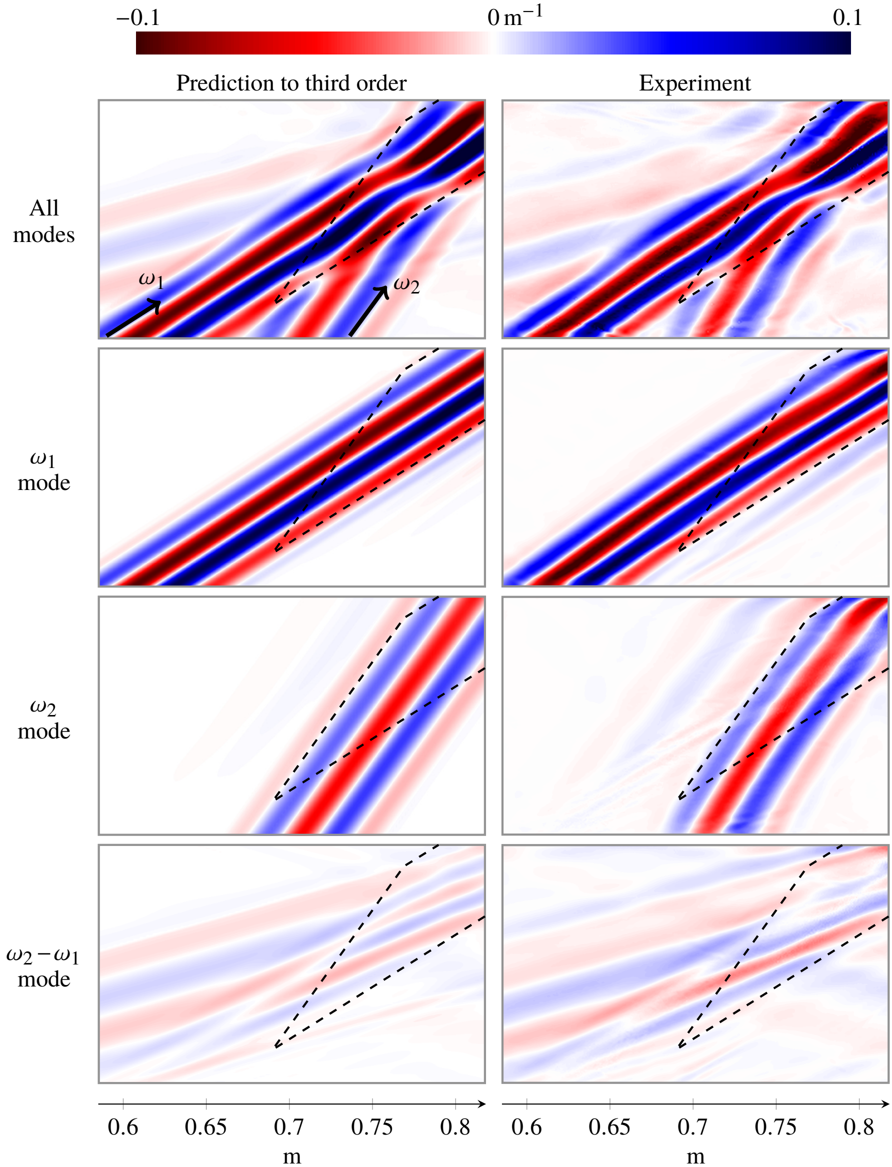

Figure 15: Decomposition of the internal wave field where $\omega_1 \approx 0.54N$ and $\omega_2 = 1.5\omega_1$. We plot the real part of evolutionary modes of the diagnostic, $(1/\rho_{00})\,\partial\rho'/\partial z$, and for reference mark the parallelogram where the incident waves cross with dotted lines. We observe that beams 1 and 2 exhibit broadening at third order.

those of beam 1. Of the remaining contributions to ω_1, we distinguish between the following permutations: the standard pairings of $-(\omega_2 - \omega_1)+\omega_2$ and $(\omega_2 + \omega_1)-\omega_2$, and an additional possible interaction, $(\omega_2 - \omega_1)-\omega_1$, whose frequency coincides with ω_1 in this configuration. It turns out that the additional interaction produces a wave that propagates down and to the left, whereas the standard pairings produce waves that propagate in the same direction as beam 1 and are responsible for broadening the beam. Given this clarity, we revisit the ω_1 and ω_2 panels in figures 12 and 13, and we note that the DMD shows clear distortion of ω_2. Although we underpredict the additional ω_2 contribution, further numerical investigations have confirmed that this third-order contribution is primarily responsible for the observed distortion of phase. Other less significant factors are due to slight curvature of the stratification, which causes waves to refract.

Returning to figure 14, at third order in ω_2, a weak wave is emitted down and to the left, which we have determined from source terms must arise from the interaction $(\omega_2 - \omega_1) + \omega_1$. Furthermore, the $\omega_2 - \omega_1$ beam is broader than the main interaction zone in a manner analogous to the broadening of ω_1, and we attribute this to higher-order contributions.

It is of interest that the wavevector of the signal in the top-right of the $\omega_2 - \omega_1$ experimental image is not aligned with the direction given by the dispersion relation, so we conclude that these are forced oscillations. Since no other wave beams intersect beam 1 in this region, we deduce that these forced oscillations must be driven by the interaction of beam 1 with itself, but a single inviscid wave cannot self-interact because its gradients are strictly normal to its velocities. If a process, such as viscous spreading of the wave beam, were to cause the direction of some wavevectors to vary, triadic interactions would then be possible. We consider the sum of two modulated modes. Should the variations in direction be small, the wavevectors of the sources must point approximately in the direction of $2\boldsymbol{k}_1$, and thus these wavevectors would be narrowly distributed about the resonant locus at the fundamental frequency, ω_1, represented by a straight line through the origin. These wavevectors would not intersect the resonant locus of the second harmonic, which is also a straight line through the origin but has steeper gradient, and thus no propagating waves would be emitted at $2\omega_1$. We hypothesise that such viscous mechanisms are responsible for these features, and in general, these are likely to be strongest close to the magic carpet. Indeed, in the $3\omega_1$ DMD mode of figure 13, we notice the same feature and attribute viscous action to its appearance.

Figure 15 shows an oblique interaction where the $\omega_2 - \omega_1$ beam is emitted back into the same quadrant from which the incident waves originate. Once again, the interactions are strong, and we successfully capture third-order beam-broadening contributions to both ω_1 and ω_2. Furthermore, we find shifts in phase to the left of the main interaction zone at both ω_2 and $\omega_2 - \omega_1$, and a propagating beam down and to the right at $\omega_2 - \omega_1$. This frequency includes both second- and third-order effects because again $\omega_2 = 1.5\omega_1$. In the top-left of the DMD mode at this frequency, there is another weak wave that we attribute to a higher-order interaction. Finally, we remark that in this experiment, it turned out that there was a smooth, weak variation in buoyancy frequency from top to bottom.

6. Conclusions

We have developed a robust hierarchically organised prediction tool for arbitrarily complex two-dimensional internal wave systems and contend that this is a necessary and sufficient model for determining the structure of wave–wave interactions near the inviscid limit. In this work, we introduce for the first time the fusion of a weakly nonlinear perturbation expansion with a semi-analytical implementation of the monochromatic free-space Green's function for the governing equation. Our method has indeed been shown to accurately recover the structure of wave–wave interactions, showing a remarkable level of agreement between our experiments and our method. Having carefully validated our approach using frequency-decomposed post-processing, we have now been able to identify wave–wave interactions up to third order by direct comparison and infer the origins of other features observed in experiments that must arise from higher orders or from secondary effects. This unparalleled access to individual components and isolation of interaction behaviour provides clarity to the mechanisms in the system, and we have attempted to explain with reference to the weakly nonlinear perturbation expansion previously unnoticed physical features, such as forced oscillations that share a frequency with other waves but do not satisfy the dispersion relation for a wave to form. Furthermore, we have strong evidence of a previously undiscovered open question regarding the order-to-order transmission efficiency of wave–wave interactions.

As necessitated by our choice of experimental validation, we have already generalised our approach to aperiodic configurations and arbitrary time dependence. With careful consideration of causality, we have also provided our calculations for a range of boundary conditions for two field potentials so that our free-space source implementation is suitable for bounded flows and, in particular, for our case that includes a flexible boundary. We have configured our implementation to be minimally elaborate while remaining causal.

We remark that there is no particular restriction to systems of internal waves. Our hierarchical decomposition is equally valid for any system for which a Green's function may be obtained. These include gravito-inertial systems, Rossby waves and some aspects of nonlinear acoustics. Further generalisations we envisage could include solving the linear inverse problem to determine suitable source strengths equivalent to a boundary displacement computed from data observed at a distance. Our experimental and numerical study has already led us to new insights on specific systems, and we anticipate the approach will be adopted for a much broader range of problems in the imminent future.

Appendix A. Derivation of monochromatic Green's function

Repurposing the method of Hurley (1972, 1997), we first calculate the Green's function for evanescent oscillations at $\omega > N$, then analytically continue it to other values of ω. Defining the transformed coordinates to perform a dilatation,

$$\begin{bmatrix} x \\ z \end{bmatrix} \mapsto \begin{bmatrix} x_\alpha \\ z_\alpha \end{bmatrix} = \begin{bmatrix} \frac{x}{\Gamma} \\ z \end{bmatrix}, \tag{A 1}$$

the point-forced internal wave equation (3.3) becomes Poisson's equation in the new coordinate system for $\omega > N$,

$$\frac{\partial^2 G_\omega}{\partial x_\alpha^2} + \frac{\partial^2 G_\omega}{\partial z_\alpha^2} = -\frac{\delta\left(x_\alpha - \frac{x_0}{\Gamma}\right)\delta(z_\alpha - z_0)}{\Gamma\omega^2}. \tag{A 2}$$

Thus, G_ω is proportional to the corresponding free-space Green's function,

$$G_\omega = C - \frac{\log\left(r^2\right)}{4\pi\omega^2\Gamma}, \tag{A 3}$$

where $r^2 = (x - x_0)^2/(1 - (N/\omega)^2) + (z - z_0)^2$ and C is the integration constant, which is a gauge freedom that we take to be zero.

We now extend G_ω to be valid at all frequencies using analytic continuation in complex ω space. The logarithm has branch points at $r^2 = \{0, \infty\}$, which rearranges to

$$1 - \left(\frac{N}{\omega}\right)^2 = \left\{-\left(\frac{x - x_0}{z - z_0}\right)^2, 0\right\}, \tag{A 4}$$

and thus the logarithm has four branch points,

$$\omega = \left\{\pm\frac{N}{\sqrt{1 + \left(\frac{x-x_0}{z-z_0}\right)^2}}, \pm N\right\}. \tag{A 5}$$

In addition, $1/\Gamma$ has three branch points, $\omega = \{0, \pm N\}$, so, in total, there are five distinct

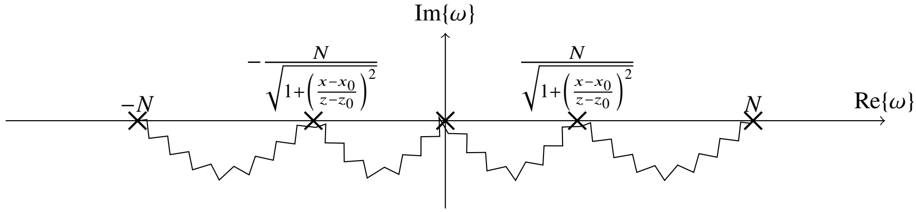

Figure 16: Branch points, shown with crosses, and branch cuts, shown with wiggly lines, for analytic continuation in ω. The five branch points are all on the real axis and the branch cut must be in the lower half plane to satisfy causality.

branch points, as marked in figure 16. Those at $\omega = \pm N$ correspond to the regime change from evanescent to propagting internal waves. The branch points all need joining with branch cuts, which we chose carefully to provide physically realisable conditions. Since any steady-state internal wave must have grown from a stationary ambient at some time in the past, we assume that the wave is in fact growing exponentially slowly in time and so $\mathrm{Im}\{\omega\} > 0$ (Lighthill 1960). Thus, we deform all the branch cuts to below the real line; these are shown by the wiggly lines in the figure.

To perform the analytic continuation, we consider the complex arguments of the square root in Γ and of the logarithm. For complex $\omega = \omega_r + \mathrm{i}\epsilon$ with real part ω_r and a small imaginary part ϵ, we make the expansion

$$\frac{1}{\Gamma^2} = \frac{1}{1-\left(\frac{N}{\omega_r+\mathrm{i}\epsilon}\right)^2} = \frac{\omega_r^2\left(\omega_r^2-N^2\right)+\left(2\omega_r^2+N^2\right)\epsilon^2+\epsilon^4-2\mathrm{i}N^2\omega_r\epsilon}{\left(\omega_r^2-N^2-\epsilon^2\right)^2+4\omega_r^2\epsilon^2}. \tag{A 6}$$

The denominator is always positive and $\epsilon \geqslant 0$, so $\mathrm{sgn}\,(\mathrm{Im}\{1/\Gamma^2\}) = -\,\mathrm{sgn}\,(\mathrm{Re}\{\omega\})$.

When $\omega > N$ and is real, the complex argument, $\arg\,(r^2) = 0$. On proceeding around the first branch point at $\omega = N$, where r^2 becomes infinite, $\mathrm{Im}\{1/\Gamma^2\} < 0$, so $\mathrm{Im}\{r^2\} < 0$. Thus, $\arg\,(r^2)$ decreases to become $-\pi$ for $N(1+((x-x_0)/(z-z_0))^2)^{-1/2} < \omega < N$; in other words, r^2 increases from $-\infty$ to zero between these branch points. As ω decreases further, the term $(x-x_0)^2/(1-(N/\omega)^2)$ becomes less significant, such that r^2 becomes positive real again after the next branch point, $N(1+((x-x_0)/(z-z_0))^2)^{-1/2}$, with its argument yet to be determined. Since $\mathrm{Re}\{\omega\} > 0$, we have $\mathrm{Im}\{1/\Gamma^2\} < 0$ and hence $\mathrm{Im}\{r^2\} < 0$, so $\arg\,(r^2)$ increases around the branch point to become zero for $-N(1+((x-x_0)\,/\,(z-z_0))^2)^{-1/2} < \omega < N(1+((x-x_0)\,/\,(z-z_0))^2)^{-1/2}$. The frequency, ω, is now negative for the remaining two branch points of the logarithm, so the analytic continuation is in the upper half ω plane. Therefore, $\arg\,(r^2) = +\pi$ for $-N < \omega < -N(1+((x-x_0)\,/\,(z-z_0))^2)^{-1/2}$ and zero for $\omega < -N$. Thus, $\mathrm{Re}\{r^2\}$ exhibits even symmetry about $\omega = 0$ but $\arg\,(r^2)$ has odd symmetry. The value of the logarithm can now be determined using the standard formula,

$$\log\left(r^2\right) = \log\left|r^2\right| + \mathrm{i}\arg\left(r^2\right). \tag{A 7}$$

Next, we consider the three branch points of $1/\Gamma$. For $\omega > N$, its complex argument is zero. Proceeding round the first branch point, at $\omega = N$, $\arg\,(1/\Gamma^2)$ decreases to $-\pi$, so $\arg\,(1/\Gamma) = -\pi/2$ and $1/\Gamma = -\mathrm{i}((N/\omega)^2-1)^{-1/2}$ for $0 < \omega < N$. The second branch point is at $\omega = 0$. When $\epsilon > 0$, $\mathrm{Im}\{1/\Gamma^2\} = 0$ only when $\mathrm{Re}\{\omega\} = 0$. At this point, $\mathrm{Re}\{1/\Gamma^2\} = \epsilon^2/(N^2+\epsilon^2) > 0$, despite being negative when ω is significantly away from zero. Thus, the analytic continuation path in complex $1/\Gamma^2$ space goes anticlockwise around the branch point, as shown in figure 17. So, $\arg\,(1/\Gamma^2) = +\pi$ for $-N < \omega < 0$, thus $1/\Gamma$

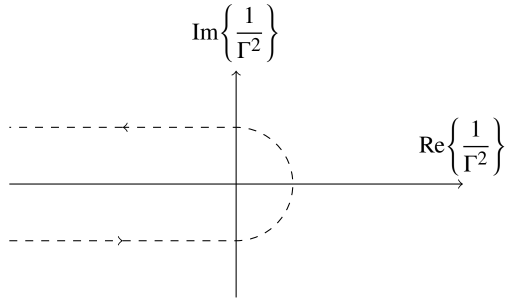

Figure 17: Analytic continuation path of $1/\Gamma^2$ for decreasing ω around 0. In order to satisfy causality, $\mathrm{Im}\{\omega\} \geqslant 0$, so the path shown is obtained by deforming ω into the upper half plane. The quantity $1/\Gamma^2$ is real and negative around $\omega = 0$, but the argument of $1/\Gamma$ changes from $-\pi$ to $+\pi$.

changes sign at $\omega = 0$. At the final branch point, $\omega = -N$, $\mathrm{Im}\{1/\Gamma^2\} > 0$, so its argument decreases from $+\pi$ to zero.

The assembled Green's function for each case is listed in table 3.

REFERENCES

Balmforth, Neil J. & Peacock, Thomas 2009 Tidal Conversion by Supercritical Topography. *J. Phys. Oceanogr.* **39** (8), 1965–1974.

Benielli, Dominique & Sommeria, Joël 1998 Excitation and breaking of internal gravity waves by parametric instability. *J. Fluid Mech.* **374**, 117–144.

Bourget, Baptiste, Dauxois, Thierry, Joubaud, Sylvain & Odier, Philippe 2013 Experimental study of parametric subharmonic instability for internal plane waves. *J. Fluid Mech.* **723**, 1–20.

Bourget, Baptiste, Scolan, Hélène, Dauxois, Thierry, Le Bars, Michael, Odier, Philippe & Joubaud, Sylvain 2014 Finite-size effects in parametric subharmonic instability. *J. Fluid Mech.* **759**, 739–750.

Dalziel, Stuart B., Hughes, Graham O. & Sutherland, Bruce R. 1998 Synthetic schlieren. In *Proc. 8th Int. Symp. Flow Vis.* (ed. Carlomagno & Grant). Paper 062.

Dalziel, S B, Hughes, G O & Sutherland, B R 2000 Whole-field density measurements by 'synthetic schlieren'. *Exp. Fluids* **28** (4), 322–335.

Dalziel, Stuart B., Patterson, Michael D., Caulfield, C. P. & Le Brun, Stéphane 2011 The structure of low-Froude-number lee waves over an isolated obstacle. *J. Fluid Mech.* **689**, 3–31.

Dalziel Research Partners 2018 DigiFlow vv3.6.0–4.2.0. http://www.dalzielresearch.com/digiflow/.

Dauxois, Thierry, Joubaud, Sylvain, Odier, Philippe & Venaille, Antoine 2018 Instabilities of Internal Gravity Wave Beams. *Annu. Rev. Fluid Mech.* **50**, 131–156.

Davis, Russ E. & Acrivos, Andreas 1967 The stability of oscillatory internal waves. *J. Fluid Mech.* **30** (4), 723–736.

Dobra, Thomas Edward 2018 Nonlinear Interactions of Internal Gravity Waves. PhD thesis, University of Bristol.

Dobra, Thomas E., Lawrie, Andrew G. W. & Dalziel, Stuart B. 2019 The magic carpet: an arbitrary spectrum wave maker for internal waves. *Exp. Fluids* **60** (11), 172.

Dobra, Thomas E., Lawrie, Andrew G. W. & Dalziel, Stuart B. 2021 Harmonics from a magic carpet. *J. Fluid Mech.* **911**, A29.

Fortuin, J. M. H. 1960 Theory and application of two supplementary methods of constructing density gradient columns. *J. Polym. Sci.* **44**, 505–515.

Görtler, H. 1943 Über eine Schwingungserscheinung in Flüssigkeiten mit stabiler Dichteschichtung. *ZAMM - Zeitschrift für Angew. Math. und Mech.* **23** (2), 65–71.

Gostiaux, Louis, Didelle, Henri, Mercier, Stephane & Dauxois, Thierry 2007 A novel internal waves generator. *Exp. Fluids* **42** (1), 123–130.

Range of ω	Argument of r^2	Argument of $\frac{1}{\Gamma}$	Green's function
$\omega > N$	0	0	$-\dfrac{\log\left(\frac{(x-x_0)^2}{1-\left(\frac{N}{\omega}\right)^2}+(z-z_0)^2\right)}{4\pi\omega^2\sqrt{1-\left(\frac{N}{\omega}\right)^2}}$
$\dfrac{N}{\sqrt{1+\left(\frac{x-x_0}{z-z_0}\right)^2}} < \omega < N$	$-\pi$	$-\dfrac{\pi}{2}$	$\mathrm{i}\dfrac{\left\{\log\left(\frac{(x-x_0)^2}{\left(\frac{N}{\omega}\right)^2-1}-(z-z_0)^2\right)-\mathrm{i}\pi\right\}}{4\pi\omega^2\sqrt{\left(\frac{N}{\omega}\right)^2-1}}$
$0 < \omega < \dfrac{N}{\sqrt{1+\left(\frac{x-x_0}{z-z_0}\right)^2}}$	0	$-\dfrac{\pi}{2}$	$\mathrm{i}\dfrac{\log\left(-\frac{(x-x_0)^2}{\left(\frac{N}{\omega}\right)^2-1}+(z-z_0)^2\right)}{4\pi\omega^2\sqrt{\left(\frac{N}{\omega}\right)^2-1}}$
$-\dfrac{N}{\sqrt{1+\left(\frac{x-x_0}{z-z_0}\right)^2}} < \omega < 0$	0	$+\dfrac{\pi}{2}$	$-\mathrm{i}\dfrac{\log\left(-\frac{(x-x_0)^2}{\left(\frac{N}{\omega}\right)^2-1}+(z-z_0)^2\right)}{4\pi\omega^2\sqrt{\left(\frac{N}{\omega}\right)^2-1}}$
$-N < \omega < -\dfrac{N}{\sqrt{1+\left(\frac{x-x_0}{z-z_0}\right)^2}}$	$+\pi$	$+\dfrac{\pi}{2}$	$-\mathrm{i}\dfrac{\left\{\log\left(\frac{(x-x_0)^2}{\left(\frac{N}{\omega}\right)^2-1}-(z-z_0)^2\right)+\mathrm{i}\pi\right\}}{4\pi\omega^2\sqrt{\left(\frac{N}{\omega}\right)^2-1}}$
$\omega < -N$	0	0	$-\dfrac{\log\left(\frac{(x-x_0)^2}{1-\left(\frac{N}{\omega}\right)^2}+(z-z_0)^2\right)}{4\pi\omega^2\sqrt{1-\left(\frac{N}{\omega}\right)^2}}$

Table 3: Monochromatic Green's function, including results of analytic continuation, for all cases of ω. An integration constant can be added onto the Green's function, but this does not affect derived quantities such as the velocity, so without loss of generality we take it to be zero.

van Haren, Hans, Maas, Leo & van Aken, Hendrik 2002 On the nature of internal wave spectra near a continental slope. *Geophys. Res. Lett.* **29** (12), 57.

Hurley, D. G. 1969 The emission of internal waves by vibrating cylinders. *J. Fluid Mech.* **36** (4), 657–672.

Hurley, D. G. 1972 A general method for solving steady-state internal gravity wave problems. *J. Fluid Mech.* **56** (4), 721–740.

Hurley, D. G. 1997 The generation of internal waves by vibrating elliptic cylinders. Part 1. Inviscid solution. *J. Fluid Mech.* **351**, 105–118.

Hurley, D. G. & Keady, G. 1997 The generation of internal waves by vibrating elliptic cylinders. Part 2. Approximate viscous solution. *J. Fluid Mech.* **351**, 119–138.

Javam, A., Imberger, J. & Armfield, S. W. 2000 Numerical study of internal waveâĂŞwave interactions in a stratified fluid. *J. Fluid Mech.* **415**, 65–87.

Jiang, Chung-Hsiang & Marcus, Philip S. 2009 Selection Rules for the Nonlinear Interaction of Internal Gravity Waves. *Phys. Rev. Lett.* **102**, 124502.

Karimi, Hussain H & Akylas, T R 2014 Parametric subharmonic instability of internal waves: locally confined beams versus monochromatic wavetrains. *J. Fluid Mech* **757**, 381–402.

Koudella, C. R. & Staquet, Chantal 2006 Instability mechanisms of a two-dimensional progressive internal gravity wave. *J. Fluid Mech.* **548**, 165–196.

Lighthill, M. J. 1960 Studies on Magneto-Hydrodynamic Waves and other Anisotropic Wave Motions. *Philos. Trans. R. Soc. A Math. Phys. Eng. Sci.* **252** (1014), 397–430.

Lighthill, M. J. 1978 *Waves in Fluids*. Cambridge University Press.

Martin, S., Simmons, W. F. & Wunsch, C. I. 1969 Resonant Internal Wave Interactions. *Nature* **224** (5223), 1014–1016.

McComas, C. Henry & Bretherton, Francis P. 1977 Resonant interaction of oceanic internal waves. *J. Geophys. Res.* **82** (9), 1397–1412.

McEwan, A. D. 1971 Degeneration of resonantly-excited standing internal gravity waves. *J. Fluid Mech.* **50** (3), 431–448.

McEwan, A. D. 1973 Interactions between internal gravity waves and their traumatic effect on a continuous stratification. *Boundary-Layer Meteorol.* **5** (1-2), 159–175.

McEwan, A. D. & Robinson, R. M. 1975 Parametric instability of internal gravity waves. *J. Fluid Mech.* **67** (4), 667–687.

Mercier, Matthieu J., Garnier, Nicolas B. & Dauxois, Thierry 2008 Reflection and diffraction of internal waves analyzed with the Hilbert transform. *Phys. Fluids* **20**, 086601.

Mercier, Matthieu J., Martinand, Denis, Mathur, Manikandan, Gostiaux, Louis, Peacock, Thomas & Dauxois, Thierry 2010 New wave generation. *J. Fluid Mech.* **657**, 308–334.

Mowbray, D. E. & Rarity, B. S. H. 1967 A theoretical and experimental investigation of the phase configuration of internal waves of small amplitude in a density stratified liquid. *J. Fluid Mech.* **28** (1), 1–16.

Müller, Peter, Holloway, Greg, Henyey, Frank & Pomphrey, Neil 1986 Nonlinear interactions among internal gravity waves. *Rev. Geophys.* **24** (3), 493–536.

Oster, Gerald 1965 Density Gradients. *Sci. Am.* **213** (2), 70–76.

Pétrélis, François, Smith, Stefan Llewellyn & Young, W. R. 2006 Tidal Conversion at a Submarine Ridge. *J. Phys. Oceanogr.* **36** (6), 1053–1071.

Phillips, O. M. 1960 On the dynamics of unsteady gravity waves of finite amplitude. *J. Fluid Mech.* **9** (2), 193–217.

Rattray, Maurice 1960 On the Coastal Generation of Internal Tides. *Tellus* **12** (1), 54–62.

Robinson, R. M. 1969 The effects of a vertical barrier on internal waves. *Deep Sea Res. Oceanogr. Abstr.* **16** (5), 421–429.

Scase, M. M. & Dalziel, S. B. 2004 Internal wave fields and drag generated by a translating body in a stratified fluid. *J. Fluid Mech.* **498**, 289–313.

Schmid, Peter J. 2010 Dynamic mode decomposition of numerical and experimental data. *J. Fluid Mech.* **656**, 5–28.

Sekerzh-Zen'kovich, S. Ia. 1981 Construction of the fundamental solution for the operator of internal waves. *J. Appl. Math. Mech.* **45** (2), 192–198.

Smith, S. & Crockett, J. 2014 Experiments on nonlinear harmonic wave generation from colliding internal wave beams. *Exp. Therm. Fluid Sci.* **54**, 93–101.

Sun, Haili & Kunze, Eric 1999*a* Internal WaveâĂŞWave Interactions. Part I: The Role of Internal Wave Vertical Divergence. *J. Phys. Oceanogr.* **29** (11), 2886–2904.

Sun, Haili & Kunze, Eric 1999*b* Internal WaveâĂŞWave Interactions. Part II: Spectral Energy Transfer and Turbulence Production. *J. Phys. Oceanogr.* **29** (11), 2905–2919.

Susanto, R. Dwi, Mitnik, Leonid & Zheng, Quanan 2005 Ocean internal waves observed in the Lombok Strait. *Oceanography* **18** (4), 80–87.

Sutherland, B. R., Dalziel, S. B., Hughes, G. O. & Linden, P. F. 1999 Visualization and measurement of internal waves by 'synthetic schlieren'. Part 1. Vertically oscillating cylinder. *J. Fluid Mech.* **390**, 93–126.

Sveen, J. K. & Dalziel, S. B. 2005 A dynamic masking technique for combined measurements of PIV and synthetic schlieren applied to internal gravity waves. *Meas. Sci. Technol.* **16** (10), 1954–1960.

Tabaei, Ali & Akylas, T. R. 2003 Nonlinear internal gravity wave beams. *J. Fluid Mech.* **482**, 141–161.

Tabaei, Ali, Akylas, T. R. & Lamb, Kevin G. 2005 Nonlinear effects in reflecting and colliding internal wave beams. *J. Fluid Mech.* **526**, 217–243.

Thorpe, S. A. 1966 On wave interactions in a stratified fluid. *J. Fluid Mech.* **24**, 737–751.

Voisin, Bruno 1991 Internal wave generation in uniformly stratified fluids. Part 1. Green's function and point sources. *J. Fluid Mech.* **231**, 439–480.

Voisin, Bruno 1994 Internal wave generation in uniformly stratified fluids. Part 2. Moving point sources. *J. Fluid Mech.* **261**, 333–374.